Physics – Uspekhi **55** (4) 382 – 407 (2012) © 2012 Uspekhi Fizicheskikh Nauk, Russian Academy of Sciences

INSTRUMENTS AND METHODS OF INVESTIGATION PACS numbers: **61.46.–w**, **62.25.–g**, **81.07.–b**, 81.07.Oj

Nanomechanical resonators

Ya S Greenberg, Yu A Pashkin, E Il'ichev

DOI: 10.3367/UFNe.0182.201204c.0407

Contents

Abstract. We review the current state of research into the development of nanomechanical resonators and their application as components of nanoelectromechanical and optomechanical systems for the highly sensitive detection and visualization of material structure. Methods for the manufacture and characterization of nanoscale mechanical resonators are described. We discuss quantum properties of nanomechanical resonators and dynamical cooling schemes for suppressing fluctuations in order to increase the threshold sensitivity of optomechanical and electromechanical systems.

1. Introduction

The development of nanothechnologies revived the interest in mechanical devices that had been used in physical experiments at the dawn of the scientific method. An example is a torsion pendulum that in 1785 enabled Coulomb to formulate the law governing the interaction of electric charges, named after him. Another example is the Cavendish experiment (1798) with the use of a torsion balance to measure the gravitational force between two lead balls.

Today, micro- and nanoscale electromechanical systems are extensively used in basic research. Their threshold force and mass sensitivities are extremely high compared to those of old mechanical devices, reaching a few zeptonewtons (1 zN $= 10^{-21}$ N) and a few zeptograms (1 zg $= 10^{-21}$ g). Using such tiny sensors, it is possible to study processes at the atomic level, e.g., to measure forces acting between individual biomolecules, magnetic fields of individual nuclear spins, masses of individual molecules and atoms, and so on.

This paper is organized as follows. Section 2 is an analytical review of developments and applications of nanoelectronic and nanomechanical systems in basic and applied research. Specifically, it describes the principal methods for the fabrication of nanomechanical resonators and the measurement of their physical characteristics. The dynamic and fluctuation properties of nanomechanical resonators and their application for the detection of ultrasmall masses and ultrasmall displacements are analyzed. The results of recent studies on the application of carbon nanotubes and graphene as nanoelectromechanical devices are presented.

Section 3 presents examples of the application of micro- and nanoscale cantilevers for the visualization of material structure. Special emphasis is laid on the operating principles and resolution of the magnetic resonance force microscope. Applications of cantilevers as ultrasensitive biosensors and as

Ya S Greenberg Novosibirsk State Technical University, prosp. K Marksa 20, 630092 Novosibirsk, Russian Federation
E-mail: yakovgreenberg@yahoo.com
Yu A Pashkin NEC Green Innovation Research Laboratories and RIKEN Advanced Science Institute, Tsukuba, Ibaraki 305-8501, Japan;
Department of Physics, Lancaster University, Lancaster, LA1 4YB, UK;
Lebedev Physical Institute, Russian Academy of Sciences, Leninskii prosp. 53, 119991 Moscow, Russian Federation
E-mail: pashkin@zp.jp.nec.com
E Il'ichev Institute of Photonic Technology (IPHT), D-07702, Jena, Germany
E-mail: evgeni.ilichev@ipht-jena.de

Received 21 May 2011, revised 4 November 2011
Uspekhi Fizicheskikh Nauk **182** (4) 407 – 436 (2012)
DOI: 10.3367/UFNr.0182.201204c.0407
Translated by Yu V Morozov; edited by A M Semikhatov

detectors of ultraweak magnetic fields generated by nuclear spins are reviewed.

The quantum mechanical properties of nanomechanical resonators are considered in Section 4, with special reference to thermodynamic quantum fluctuations and their influence on threshold sensitivity. Measurement systems allowing the so-called standard quantum limit to be reached are presented; the possibility of overcoming this limit is discussed. Various methods for the cooling of micro- and nanomechanical resonators in nanoelectromechanical and optomechanical systems are described.

2. Applications of nanoscale electromechanical systems

2.1 Introductory notes

The creation of new solid-state structures ranging from a few nanometers to a few hundred nanometers opens up a novel sphere of basic and applied research. Mechanical and electronic nanostructures, such as carbon nanotubes, nanowires, and nanomechanical resonators made from semiconducting and metallic materials, provide a basis for future nanoelectronic, nanoelectromechanical, and photonic integrated circuits for ultrasensitive sensors, quantum information processing devices, and other instruments suitable for a variety of applications, from reliable ultrafast communication systems to biomedicine. Realization of these applications requires the knowledge of the properties of nanomechanical devices and their controllable manipulation. For this, a measurement and control system must be developed to enable conversion of information on the location of a nanoobject into electric signals and vice versa. The systems containing electronic and mechanical components are usually composed of an electron module and a set of mechanoelectrical nanosensors and/or electromechanical transducers (actuators), generally called nanoelectromechanical systems (NEMSs).

Considerable progress has been achieved in the development of NEMSs. They include nanomechanical resonators ranging in size from tens to hundreds of nanometers and having unique characteristics, for example, the fundamental frequency varying from a few MHz to tens of GHz, a mechanical quality factor amounting to tens of thousands, an active mass of several femtograms (10^{-15} g), and a dissipated power of several attowatts (10^{-17} W) [1]. Thus far, the following threshold sensitivities of NEMSs have been reached: displacements 2×10^{-15} m $\mathrm{Hz}^{-1/2}$ [2], mass $(10^{-18} - 10^{-19})$ g $\mathrm{Hz}^{-1/2}$ [3, 4], force 10^{-16} N $\mathrm{Hz}^{-1/2}$ [5], electric charge $10^{-1}\, e\ \mathrm{Hz}^{-1/2}$ ($e \approx 1.6 \times 10^{-19}$ is the electron charge) [6], and spatial resolution below 100 nm [7].

As follows from these data, the unique properties of NEMSs allow creating ultrasensitive measurement instruments for use in quantum metrology, scanning force microscopy, magnetic resonance imaging (MRI), etc. Moreover, ongoing developments in this field offer the possibility of applying NEMS to elucidate the electronic structure of individual molecules and controlling their motion, e.g., for the analysis of the atomic structure of nanomaterials and biomolecules.

The discovery of these properties stimulated a flood of ideas and proposals of interesting experiments and NEMS applications, from the search for gravitational waves to the manipulation of biomolecule structure. At the same time, the use of NEMSs raises a number of fundamental questions that remain to be answered. They concern nanotechnological issues (reproducibility, control of surface and bulk properties), and the development of new measurement tools to study the mechanics and properties of nanoobjects at the atomic level. From the theoretical standpoint, it is important to analyze the applicability of the continuum approach to the calculation of mechanical characteristics of a resonator (to elucidate how the molecular and atomic structure of nanoobjects relates to their behavior). It follows from the above that NEMS studies are at the forefront of physical and engineering sciences, encompassing a few domains of either of them.

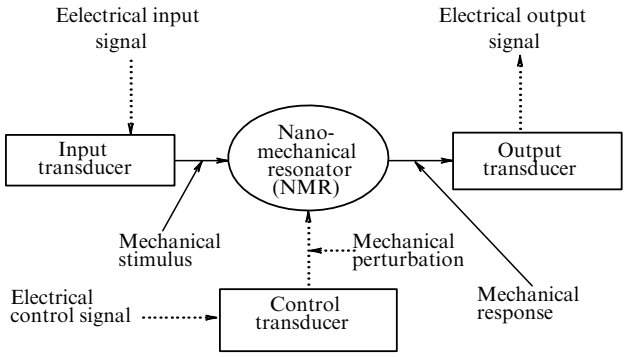

Figure 1. Block diagram of a nanoelectromechanical system.

Figure 1 shows a typical block diagram of an NEMS. Its main element is a nanomechanical resonator (NMR) excited by electrical signals via an input transducer that transforms the electric energy into the energy of mechanical vibrations of the resonator (on its first harmonic or sub-harmonics). Simultaneously, a control signal related to the study object is fed into the NMR through another transducer. This signal can carry information on the parameter being measured (e.g., object displacement or magnetic moment). The resultant signal from NMR mechanical vibrations containing the information about the parameter of interest is converted back into the electrical signal at the exit from the NMR; this signal is amplified and arrives to the detector.

We note that most developments in this realm are thus far confined to laboratory experiments. At best, we can speak only of prototypes of the future NEMSs. One such system is the magnetic resonance force microscope (MRFM) with a spatial resolution down to a few dozen nanometers, which corresponds to the threshold magnetic moment sensitivity of the order of 1000 nuclear spins [7], which is roughly 100 times better than for a conventional nuclear magnetic resonance spectrometer.

As is known, fluctuations of various types are the main factor limiting the measurement range of any instrument. For example, the threshold sensitivity of an NMR depends on thermal fluctuations, as long as the condition $\hbar\omega \ll k_{\mathrm{B}}T$ is fulfilled, where $\hbar$ is the Planck constant, ω is the resonator characteristic frequency, k_{B} is the Boltzmann constant, and T is the absolute temperature. However, thermal fluctuations at $\hbar\omega \geqslant k_{\mathrm{B}}T$ do not play a critical role, whereas fluctuations determined by the quantum properties of the sensors start to dominate. A frequency of 1 GHz corresponds to an energy attainable experimentally at 50 mK. Hence, the advent of nanoscale resonators with fundamental frequencies in the GHz range made it possible, in principle, to achieve a

fluctuation limit determined by their quantum properties. Moreover, extensive experimental and theoretical investigations are carried out in this field with the aim to develop methods for improving the sensitivity of these sensors, overcoming the aforementioned standard fluctuation quantum limits. Such methods include quantum nondemolition measurements, radiative and electromagnetic cooling, and the use of entangled and squeezed states.

2.2 Characteristics of nanomechanical resonators

Nanomechanical resonators have received increased attention in recent years because they can be used as more sensitive and energy-saving detectors than their micromechanical analogs [1, 8]. We also note that the quality factor of mechanical resonators is higher than that of electrical (nonsuperconducting) ones. The integration of an NMR into single-electron transistors [2, 9, 10], superconducting interferometers [11, 12], superconducting charge [13] and flux [14] qubits, and stripline UHF resonators [15] opens up new possibilities for investigations into the rich dynamics of integrated electromechanical systems having both mechanical and electromagnetic degrees of freedom. The coupling between these degrees of freedom can be controlled by an external signal. Such experiments permit studying quantum phenomena in hybrid electromechanical systems.

Most nanomechanical resonators are either a cantilever (a beam clamped at only one end) or a bridge (a doubly clamped beam) fabricated by submicron (electron-beam) lithography from single-crystal materials, such as Si [16–18] or SiC [19, 20].

The first nanoscale radiofrequency mechanical resonator made of single-crystal silicon was described in Ref. [16]. Being 7.7 μm long, 0.33 μm wide, and 0.8 μm thick, the resonator had the fundamental resonance frequency 70.72 MHz and $Q = 1.8 \times 10^4$. Another silicon NMR with dimensions $2 \times 0.2 \times 0.1$ μm and a frequency of 380 MHz was reported a few years later in Ref. [21]. However, the Q-factors of all the silicon NMRs studied in [21] were much smaller ($Q \sim 10^3$) than in [16]. The authors of Ref. [21] failed to identify the exact cause of the discrepancy, but suggested that the quality of the NMR surface might be involved. Specifically, it was shown in [21] that a decrease in the surface-to-volume ratio (for samples fabricated within one technological cycle) resulted in an increase in Q. A few years ago, the psychological barrier of 1 GHz for an NMR made of semiconducting materials was overcome, and a silicon carbide-based resonator with dimensions $1.1 \times 0.12 \times 0.075$ μm, the frequency 1.029 GHz, and $Q \sim 10^4$ was created [22].

Other materials studied for the same purpose included gallium arsenide (GaAs) [23, 24] (frequency ≈ 10 MHz, dimensions $6 \times 0.5 \times 0.1$ μm, $Q \sim 10^3$; see [24]); silicon nitride (Si_xN_y) [25] (frequency ≈ 100 MHz, dimensions $\approx 4 \times 0.5 \times 0.2$ μm, $Q \sim 10^3$); aluminium nitride (AlN) [26] (frequency ≈ 100 MHz, dimensions $\approx 2 \times 0.2 \times 0.2$ μm, $Q \sim 10^4$); nanocrystalline diamond (NCD) [27] (frequency ≈ 10 MHz, dimensions $\approx 1 \times 0.2 \times 0.05$ μm, $Q \sim 10^3$); and later, Q-factors $\sim 10^4$ were achieved at low temperatures [28].

Elastic deformations of solids are described by the Euler–Bernoulli theory. We consider a beam of length L and cross section A clamped at both ends and made of a material with a density ρ and Young's modulus E. The z axis is directed along the principal axis of the beam. The displacement of the beam $U(z, t)$ from the equilibrium position in the absence of an external force is described by the equation

$$\rho A \frac{\partial^2 U}{\partial t^2}(z, t) + EI_y \frac{\partial^4 U}{\partial z^4}(z, t) = 0\,, \tag{2.1}$$

where I_y is the geometric moment of inertia with respect to the y axis. If the time dependence of the displacement is assumed to be harmonic, $U(z, t) = U(z) \exp(-\mathrm{i}\omega t)$, the spatial dependence must satisfy the equation

$$\frac{\mathrm{d}^4 U}{\mathrm{d}z^4}(z) = \left(\frac{\rho A}{EI_y}\right)\omega^2 U(z)\,. \tag{2.2}$$

The general solution for the beam displacement has the form

$$U(z, t) = a\cos(\beta z) + b\sin(\beta z) + c\cosh(\beta z) + d\sinh(\beta z)\,, \tag{2.3}$$

where $\beta = (\rho A/EI_y)^{1/4}\omega^{1/2}$. This solution must satisfy four boundary conditions. For a beam clamped at both ends (at $z = 0$ and $z = L$), the displacements $U(0)$ and $U(L)$ as well as the slopes $\mathrm{d}U/\mathrm{d}z(0)$ and $\mathrm{d}U/\mathrm{d}z(L)$ are equal to zero. It follows from these boundary conditions that $a = -c$ and $b = -d$, while the parameter β takes discrete values satisfying the relation

$$\cos\beta_n L \cosh\beta_n L - 1 = 0\,. \tag{2.4}$$

The numerically found solutions of Eqn (2.4) are $\beta_n L = 0$, 4.730, 7.853, 10.996, 14.137, ... Discarding the trivial solution $\beta_n L = 0$, we arrive at the following expression for the displacement:

$$U_n = a_n\left[\cos(\beta_n z) - \cosh(\beta_n z)\right] + b_n\left[\sin(\beta_n z) - \sinh(\beta_n z)\right]\,, \tag{2.5}$$

where the amplitude ratio a_n/b_n for the first few modes is found from the boundary conditions: $a_n/b_n = 1.018$, 0.999, 1.000, ... The values of $U_n(z)$ satisfy the normalization condition

$$\int_0^L U_n(z)\, U_m(z)\, \mathrm{d}z = L^3 \delta_{mn}\,. \tag{2.6}$$

This condition yields $a_n = L$, while b_n can be found from the above relations.

The frequencies of the corresponding modes are given by

$$\omega_n = \sqrt{\frac{EI_y}{\rho A}}\,\beta_n^2\,. \tag{2.7}$$

Typically, the fundamental bending (flexural) mode of beam vibrations is measured in experiment as producing the highest signal. For the fundamental mode, $\beta_1 = 4.73/L$. Therefore, its resonance frequency is given by

$$f_1 = \frac{1}{2\pi}\frac{(4.73)^2}{L^2}\sqrt{\frac{EI_y}{\rho A}} \approx \frac{3.56}{L^2}\sqrt{\frac{EI_y}{\rho A}}\,. \tag{2.8}$$

For a resonator of a rectangular cross section, $A = wt$, where w and t are the width and the thickness of the resonator strip (in the direction of vibrations). The moment of inertia is $I_y = wt^3/12$; hence, the resonance frequency of the fundamental mode is

$$f_1 = 1.03\sqrt{\frac{E}{\rho}}\,\frac{t}{L^2}\,. \tag{2.9}$$

The frequencies of the next modes are found from the relation $f_n/f_1 = 2.756, 5.404, 8.933$ for $n = 2, 3, 4$.

It follows from (2.9) that the frequency can be increased by increasing the t/L^2 ratio or choosing stiffer (with greater E) and lighter (of low density ρ) materials.

Expression (2.8) was obtained in the absence of resonator stress. Taking the stress into account leads to the following expression for the frequency of the fundamental flexural mode [29]:

$$f_0 = \frac{2\pi}{L^2}\sqrt{\frac{EI}{3\rho A}\left(1 + \frac{L^2 T_0}{4\pi^2 EI}\right)}\,, \tag{2.10}$$

where T_0 is the residual stress, for example, due to the difference between thermal expansion coefficients of the resonator and the substrate materials.

If the resonator is clamped at one end (at $z = 0$) and free at the other ($z = L$) (cantilever), the boundary conditions have the form $U(0) = 0$, $\mathrm{d}U/\mathrm{d}z(0) = 0$, $\mathrm{d}^2U/\mathrm{d}z^2(L) = 0$, and $\mathrm{d}^3U/\mathrm{d}z^3(L) = 0$. The last two conditions ensure the absence of a transverse force and torque at the free end. In this case, the resonance frequencies are determined from the equation

$$\cos\beta_n L \cosh\beta_n L + 1 = 0\,,$$

whose solutions are $\beta_n L = 1.875, 4.694, 7.855, 10.996, \ldots$. As in the case of a resonator clamped at both ends, the shape of harmonics $U_n(z)$ is described by Eqn (2.5) with the ratios of coefficients $a_n/b_n = -1.3622, -0.9819, -1.008, -1.000, \ldots$. Apparently, the resonance frequency of a doubly clamped resonator is $(4.730/1.875)2 \approx 5.62$ times that of a resonator with one free end.

2.3 Methods for the fabrication of nanomechanical resonators

A transition from micro- to nanoscale typically implies qualitatively new technological solutions. Electron-beam lithography and dry etching become the key technological tools for dealing with nanoscale objects. Usually, NMR is first fabricated with the use of a mask on the so-called sacrificial layer from which the resonator is subsequently released by etching, while the leads of the resonator remain attached to the substrate.

The NMR fabrication process consists of several steps that we briefly describe for a silicon-based NMR [16]. Fabrication of NMRs from other materials is discussed below (see monograph [30] for more details).

The main NMR fabrication steps (1–7) are schematically shown in Fig. 2a [16]. At the initial step 1, an SiO_2 layer 1 μm thick is grown on a single-crystal Si(100) substrate to be used as a mask at the stage of Si etching. SiO_2 is spin-coated with a two-layer positive electron resist, with polymethyl methacrylate-495 (PMMA-495) forming the bottom layer and PMMA-950 the top one. At the next step, electron-beam lithography is used to form a window in the resist, whose shape determines the structure of future NMRs. Then, an Ni layer is deposited onto the substrate by evaporation. After the removal of the resist, Ni covers only the window region formed earlier at step 1. The Ni layer plays the role of a mask during subsequent etching of SiO_2. The Ni mask pattern is transferred into the SiO_2 layer by means of anisotropic reactive ion etching in the atmosphere of C_2F_6 (step 2 in Fig. 2a). Because the etch rates of SiO_2 and Si are different, the etching process practically stops after SiO_2 is removed. Then anisotropic etching of Si continues in a mixture of NF_3 and CCl_2F_2 (step 3). At this step, the future Si beam forms, its thickness being a function of the etching depth. The removal of the Ni layer is followed by pyrogenic oxidation of the side walls of the silicon structure. At the same time, SiO_2 is formed on the horizontal silicon surface (step 4). SiO_2 is removed by repeated anisotropic reactive ion etching (step 5). At the final step, silicon beneath the beam is removed by isotropic reactive ion etching in NF_3 (step 6), the etch rate of Si being virtually identical to that of the upper SiO_2 layer; hence, the importance of monitoring etch time at step 6. After the beam is released from the substrate (which is confirmed by scanning electron microscopy), the remaining SiO_2 layer is removed by diluted hydrofluoric acid and the processed samples are rinsed in deionized water. They are frequently subjected to additional metallization for measurement purposes. In such cases, the NMR is coated with a 5–10 nm adhesive Cr or Ti layer overlaid with a thicker Au or Al layer (step 7). A scanning electron micrograph of the silicon-based NMR thus obtained is presented in Fig. 2b. It shows that the bottom part of the has some scalloping, probably due to nonuniform oxidation of Si. Moreover, the Si surface etched beneath the resonator shows a protrusion, because NMR itself serves as a mask at the final step of isotropic etching.

A somewhat simpler method was used in Ref. [25] to fabricate an NMR from silicon nitride (Fig. 3). At step 1, an SiO_2 layer a few hundred nanometers in thickness is grown on a single-crystal silicon (Si(100)) substrate. It is covered with silicon nitride of roughly the same thickness, which is then spin-coated with PMMA. At the next step, the geometric structure of the future NMR is formed in the resist by

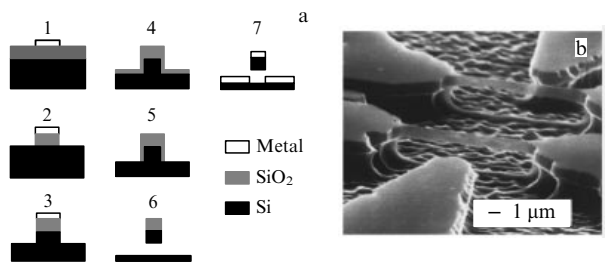

Figure 2. (a) Schematic representation of the main technological steps for the fabrication of an Si-based NMR. (b) Scanning electron micrograph of an Si-based NMR [16].

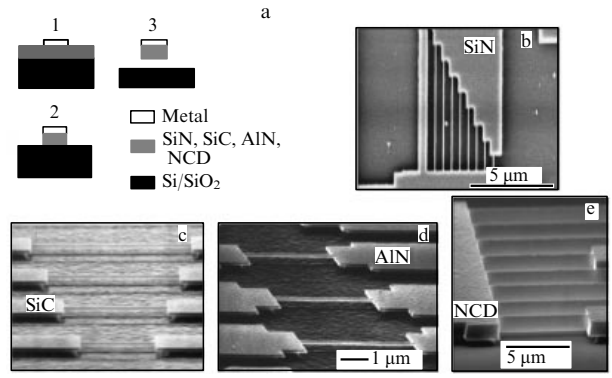

Figure 3. (a) Schematic representation of the main technological steps for the fabrication of SiN, SiC, AlN, and NCD-based NMRs [25]. Scanning electron micrograph of SiN [25] (b), SiC, [19] (c), AlN [26] (d), and NCD [32] (e) NMRs [16].

electron-beam lithography, and the entire substrate is covered with Cr by evaporation. After removal of the resist, the chromium film remains only over the window region formed in step 1. The Cr layer serves as a mask during subsequent etching of SiN. Silicon nitride is removed by plasma etching in $CH_4 - H_2$, which leaves SiN only under the Cr mask (stage 2). At the final step 3, the SiO_2 layer is removed by selective chemical etching that releases NMR from the substrate. Silicon nitride being a dielectric, the completed NMR is subjected to metallization for the purpose of measurements.

Figure 3b shows a scanning electron micrograph of an SiN-based NMR [25] 8 μm long × 200 nm wide × 100 nm thick, with a resonance frequency of 19.7 MHz. The NMR is covered with an Au layer 20 nm thick.

One more attractive material for NMR fabrication is single-crystal silicon carbide (SiC) [19, 20], in which the speed of sound $\sqrt{E/\rho}$ is roughly twice that in silicon. The technological steps for the fabrication of the SiC NMR are very similar to those used to form an SiN NMR; we therefore refer to Fig. 3a.

The fabrication of an SiC NMR requires growing a film of this material on a silicon wafer by means of chemical deposition from the high-pressure gaseous phase. This step is followed by coating a 30–60 nm thick Cr layer over SiC by electron-beam lithography; its pattern determines the shape of the future NMR (see structure 1 in Fig. 3a). This pattern is transferred into the SiC layer by anisotropic etching in an $NF_3/O_2/Ar$ mixture in an electron cyclotron resonance reactor (see structure 2 in Fig. 3a). Narrow beams formed in the SiC layer are released from the substrate by isotropic etching of Si in the same apparatus using an NF_3/Ar mixture that does not etch SiC in the absence of oxygen. The chromium mask is removed either by argon plasma or by a standard liquid etching agent. The high chemical stability and mechanical strength of the beams thus obtained allow further lithographic procedures for metallization. The metallic layer consists of a 200 nm thick Au and a 5 nm Cr sublayer (a structure resembling structure 3 in Fig. 3a). NMRs fabricated by this method are depicted in Fig. 3c.

A metallic mask is also used to fabricate NMRs from single-crystal AlN [26]. Aluminum nitride has gained the attention of researchers as a light ($\rho = 3255$ kg m^{-3}) material with a rather high Young modulus ($E = 345$ GPa). These characteristics ensure resonance frequencies higher than those for resonators of identical geometry made of some other materials.

The technological steps of resonator formation from AlN are also similar to those in the fabrication of an SiN NMR. Therefore, we again refer to Fig. 3a. At the beginning, an Si/AlN wafer is coated with a two-layer electron resist. A 3 nm thick adhesive Ti layer, 35 nm Au layer, and 60 nm Ni layer are deposited into a window formed in the resist by electron-beam lithography. After the resist with metallic layers is removed, the resulting structure looks as structure 1 in Fig. 3a. The Ni layer serves as a mask during anisotropic reactive ion etching of AlN, whereas Au forms a conductive layer for magnetomotive measurements. AlN etching performed in clorine gas (see structure 2 in Fig. 3a) is followed by the removal of Ni using a standard liquid etchant. The resonator is released from the substrate by the liquid etchant and rinsed in ethanol (see structure 3 in Fig. 3a).

Another material suitable for the fabrication of NMRs is diamond, characterized by the highest speed of sound $\sqrt{E/\rho}$, which accounts for a higher resonant frequency than in other materials with the same geometry. For example, the resonance frequency of diamond resonators is roughly thrice that of silicon ones of the same size. Moreover, diamond shows high thermal conductivity at low temperatures compared with other insulators, which allows effective thermalization of mechanical resonators.

The procedure of forming resonators from nanocrystalline diamond is as follows. A film of nanocrystalline diamond is deposited onto a pure silicon or silicon oxide substrate [31]. Both types of wafers are covered with a seed diamond nanopowder in three steps. In the case of pure silicon, these steps are (1) cleaning the substrate in an acetone ultrasonic bath, (2) immersing the substrate in the ultrasonic acetone bath containing diamond nanopowder, (3) rinsing the substrate in acetone. The diamond film is deposited at a substrate temperature of 800 °C by plasma–chemical vapor deposition using a mixture of 1% CH_4, 2%–10% H_2, and Ar. The resulting film is 400–600 nm thick. The next steps are shown in Fig. 3a.

A metal pattern is written by the lift-off process on the diamond film obtained as described in the preceding paragraph. The metal layer of Au with a sublayer of Ti and a Cr layer on top of Au resembles structure 1 in Fig. 3a. The Cr layer used as a mask in subsequent etching of the diamond film is removed upon completion of fabrication. The gold layer remains at the diamond surface to enable resonator measurements by the magnetomotive method. At the next step, a structure (the future NMR) is cut out in the diamond film by the reactive ion etching technique [32, 33]. Anisotropic diamond etching through the Cr mask in an O_2/CF_4 mixture yields a structure analogous to structure 2 in Fig. 3a. At the final stage, suspended diamond beams are formed by etching the substrate material underneath the film with buffered hydrofluoric acid (see structure 3 in Fig. 3a).

Metallic NMRs are also a subject of intense current interest because many types of transducers, e.g., single-electron transistors and SQUIDs, are also made of metal; hence, the opportunity to fabricate NMRs and these devices in one production cycle.

In what follows, we describe a method for the fabrication of NMRs from metals having a relatively low melting temperature. It was used to form NMRs from aluminum, gold, and titanium [34, 35, 39]. A limitation on the melting temperature is imposed by the use of an organic polymer in the fabrication process, which excludes the application of refractory metals such as niobium.

The main steps of fabrication of metallic nanomechanical resonators are shown in Fig. 4. First, a layer of calixarene, a negative resist, is spin-coated onto the substrate and a pedestal is formed by electron-beam lithography that serves to form a metal structure (structure 1 in Fig. 4a). Then the

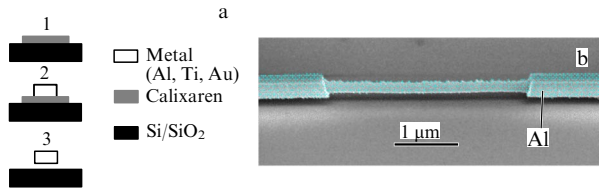

Figure 4. (a) Schematic representation of the main technological steps for the fabrication of a metallic NMR [35]. (b) Scanning electron micrograph of an Al-based NMR [35].

entire substrate is coated with a trilayer resist structure consisting of LOR3A resist, germanium, and PMMA (from bottom up). The future resonator is patterned in the PMMA layer by an electron beam and subsequent development. At the next step of reactive ion etching with CF_4, the pattern is transferred into the Ge layer. Then, the PMMA layer over Ge is removed by oxygen plasma and the LOR3a is subjected to etching through the open windows in Ge using a special RPG solution (remover PG) that does not react with calixarene. Upon metallization, the substrate is placed in RPG heated to 80 °C to remove all the layers except the metallic one deposited through the Ge mask. At this step, the structure looks like structure 2 in Fig. 4a. The fabrication is completed by ashing calixarene under the resonator in oxygen plasma (structure 3 in Fig. 4a). Calixarene is completely removed only from beneath the resonator, i.e., the narrowest part of the metal layer, but preserved as a support under the wider clamps.

As an example, Fig. 4b demonstrates a fabricated Al-based resonator of dimensions (l.w.t.) 3 μm × 100 nm× 200 nm. It is spaced 50–100 nm (the calixarene layer thickness) apart from the substrate. This imposes limitations on the resonator size. For instance, the maximum length of a 200 nm thick resonator is usually less than 5 μm, because longer ones tend to sag and adhere to the substrate.

This technology allows fabricating both a single patterned metal layer containing nanomechanical resonators and integrated multilayer, e.g., two-layer, structures [36]. Such structures consisting of a nanomechanical resonator and an electronic transducer can be regarded as two-in-one devices exemplified by a single-electron transistor whose island is suspended above the bottom gate. Its mechanical resonator is the source-to-drain part of the island, while the clamps are the source and drain electrodes that are made much thicker than the island. The conversion of mechanical vibrations into an electric signal (which is possible due to the high sensitivity of single-electron transistors to island charge variations) is described in Section 2.4.4.

2.4 Methods for measuring the characteristics of nanomechanical resonators

There are a variety of methods for measuring the characteristics of nanoscale resonators, some of which are borrowed from macroresonator studies. The most sensitive of them are used to measure mechanical vibrations of NMR in the absence of an external drive, such as those induced by thermal fluctuations. Otherwise, a resonator must be driven by an external force. In any case, mechanical vibrations must be transduced into variations of an electric signal. The transducer may be a special device located near the resonator and coupled to it one way or another. Moreover, the resonator itself can be part of an electronic (nanoelectronic) device. Finally, transformation of mechanical vibrations into variations of the electric current is possible in the absence of nearby or built-in electronic devices. The magnetomotive method is an example of such a transformation. It is the simplest and most widespread method for measuring mechanical vibrations, which was initially used in dealing with large resonators [37] and thereafter found application for nanomechanical resonators [16, 35, 38].

2.4.1 The magnetomotive method. The magnetomotive measurement setup is outlined in Fig. 5. The resonator is connected to a radiofrequency circuit and placed in a

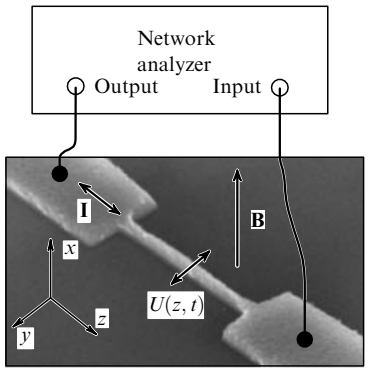

Figure 5. Schematic of NMR measurement by the magnetomotive method [35].

uniform constant magnetic field **B** normal to the resonator principal axis. A high-frequency alternating current **I** is passed through the resonator. The Lorenz force per unit length of the resonator with the passing current is

$$\mathbf{F}_{\mathrm{L}}(z) = \mathbf{I} \times \mathbf{B}\,. \tag{2.11}$$

This force is perpendicular to the magnetic field and the current flow. The dynamics of resonator bending oscillations are described by the equation of motion [30, 39]

$$\rho A\,\frac{\partial^2 U}{\partial t^2}(z,t) + EI_y\,\frac{\partial^4 U}{\partial z^4}(z,t) = F_{\mathrm{L}}(z)\exp(-\mathrm{i}\omega t)\,. \tag{2.12}$$

The shape of the first harmonic of bending oscillations $U_1(z,t)$ corresponding to a resonance at half the wavelength for a doubly clamped beam is found from Eqn (2.5) for $n = 1$ [40]. The displacement $U_1(z)$ of the resonator from the equilibrium position for an alternating current frequency ω close to the beam resonance frequency ω_0 is given by $U_1(z,t) = a_1 U_1(z)\exp(-\mathrm{i}\omega t)$, where a_1 is the dimensionless oscillation amplitude of the first harmonic,

$$a_1 = \frac{1}{\rho A L^3}\,\frac{1}{\omega_0^2 - \omega^2 - \mathrm{i}\omega_0^2/Q}\int_0^L U_1(z)\,F_{\mathrm{L}}(z)\,\mathrm{d}z\,. \tag{2.13}$$

In the case of a uniform force $F_{\mathrm{L}}(z) = F_{\mathrm{L}}$,

$$a_1 = \frac{\eta_1}{\omega_0^2 - \omega^2 - \mathrm{i}\omega_0^2/Q}\,\frac{F_{\mathrm{L}}}{m}\,,$$

where $\eta_1 = (1/L^2)\int_0^L U_1(z)\,\mathrm{d}z \approx 0.8309$ and $m = \rho A L$ is the beam mass. This means that the amplitude of beam vibrations is proportional to the applied force amplitude, which, in turn, is proportional to the passing current amplitude. This relation holds for a linear setup (at small beam deflections).

Beam displacements in a magnetic field give rise to an electromotive force (e.m.f.) V expressed as the time derivative of the magnetic flux:

$$V(\omega) = \frac{\mathrm{d}\Phi}{\mathrm{d}t} = \frac{\partial}{\partial t}\int_0^L B U_1(z,t)\,\mathrm{d}z$$
$$= -\mathrm{i}\,\frac{\omega\eta_1^2}{\omega_0^2 - \omega^2 - \mathrm{i}\omega_0^2/Q}\,\frac{I_0 B^2 L^2}{m}\exp(-\mathrm{i}\omega t)\,. \tag{2.14}$$

According to (2.14), the e.m.f. shows a quadratic dependence on the magnetic field B and a linear dependence on the alternating current amplitude I_0. These dependences have been confirmed in experiment.

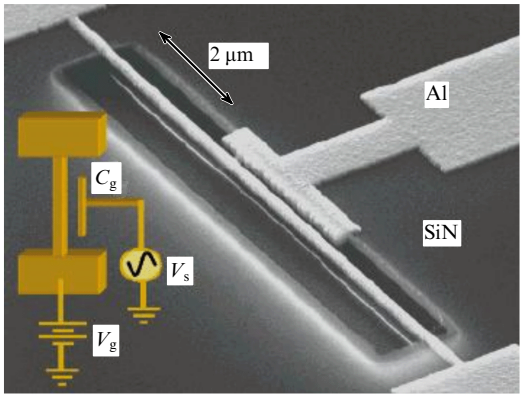

Figure 6. Schematic of NMR measurement by the electromotive method [41].

The comparison of (2.14) and the expression for the voltage in the tank circuit with parallel connection of the effective capacitance C_m, inductance L_m, and resistance R_m reveals their complete equivalence. At the resonance frequency,

$$C_m = \frac{m}{\eta_1^2 L^2 B^2}\,, \qquad L_m = \frac{\eta_1^2 L^2 B^2}{\omega_0^2 m}\,, \qquad R_m = \frac{\eta_1^2 L^2 B^2}{\omega_0 m}\,Q\,,$$

whence $\omega_0^2 = 1/(L_m C_m)$. Measurement of a radiofrequency RF signal passing through the beam by a network analyzer yields a transmission coefficient with a characteristic dip at the beam resonance frequency.

2.4.2 The electromotive (capacitive) method. The electromotive method is outlined in Fig. 6 [41]. A nanomechanical resonator is capacitively coupled to a gate to which an RF signal is applied to induce vibrations with an amplitude depending on the signal frequency. It can be shown that the NMR at resonance is equivalent to a series-connected array of capacitance, inductance, and resistance with the effective values

$$C_m = \frac{V_g^2 C_g^2}{\omega_0^2 d^2 M}\,, \qquad L_m = \frac{d^2 M}{V_g^2 C_g^2}\,, \qquad R_m = \frac{d^2 M \omega_0}{V_g^2 C_g^2 Q}\,.$$

The gap impedance Z between the resonator and the gate depends on the resonator displacement: $|Z| = 1/(\omega C_g)$ off resonance and $|Z| \approx R_m$ at resonance. In the measurements, a resonant tank circuit connected in parallel with the NMR is used to match the high impedance $|Z|$ (typically higher than 100 kΩ) and a 50 Ω measurement circuit. Then, under the condition that the frequency of the tank circuit matches the NMR frequency, the total impedance at the resonance frequency is $Z_{tot} \approx Z_{LC}^2/R_m + R_T$, where $Z_{LC} = \sqrt{L_T/C_T}$ is the characteristic impedance of the circuit and R_T is its ohmic losses. Ideally, when Z_{tot} is close to 50 Ω, practically all high-frequency power is transferred into the NMR, leading to the appearance of a characteristic feature in the signal reflected from the HF circuit. This peculiarity is a measure of the NMR resonance frequency and the Q-factor.

An advantage of this method is the possibility of measuring a few NMRs simultaneously if their frequencies fall into the operating bandwidth of the tank circuit. The threshold sensitivity to a mechanical displacement of 4.1×10^{-12} m Hz$^{-1/2}$ at $V_g = 15$ V demonstrated in Ref. [41] depended on losses in the tank circuit.

2.4.3 Investigations of thermal fluctuations of a nanomechanical resonator by an atomic point contact. In this method, a tunnel junction between a mechanical resonator and the tip of an atomic point contact serves to transduce mechanical vibrations into variations in the electrical current. Measurements by this technique are schematically illustrated in Fig. 7. Its application is limited to conductive materials that do not form surface oxides. The sole experiment with the use of this method reported in Ref. [39] was carried out with a gold NMR to the middle of which another gold

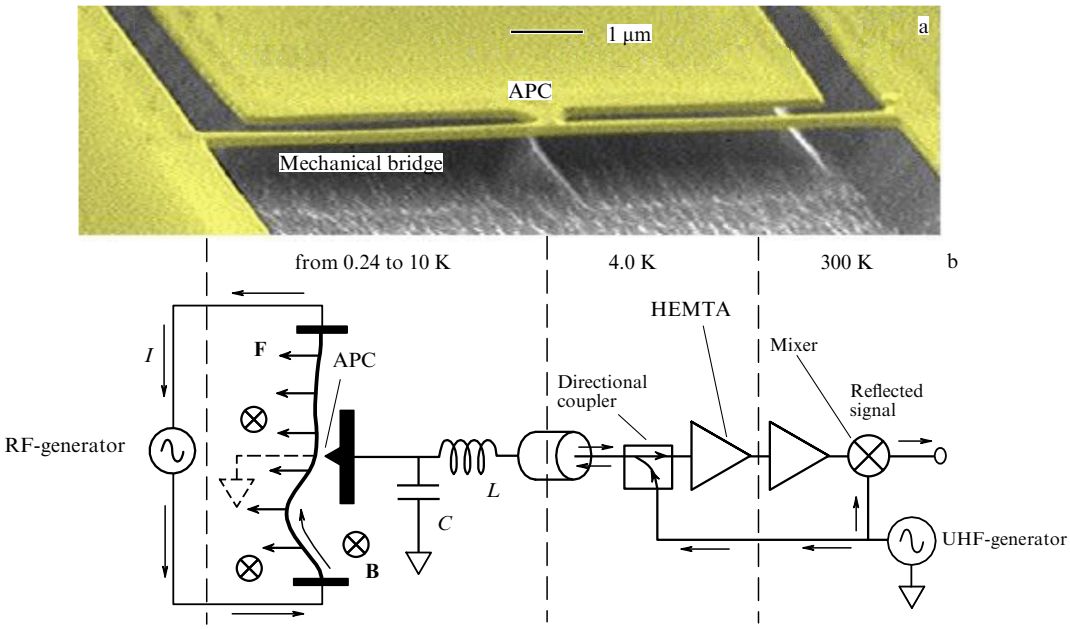

Figure 7. (a) Scanning electron micrograph of a gold-based nanomechanical resonator. (b) Circuit schematic for atomic point contact (APC) measurement of its vibrations; HEMTA is a high electron mobility transistor amplifier [39].

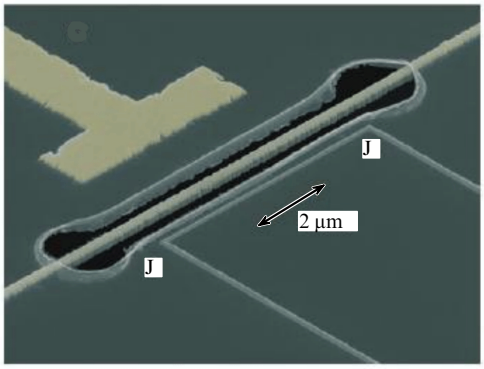

Figure 8. Scanning electron micrograph of a nanomechanical resonator (8 μm × 200 nm) formed from a 100 nm thick SiN film with a conductive coating of Au 20 nm in thickness. The island of the single-electron transistor (5 μm long, 50 nm wide) spaced 600 nm apart from the resonator forms two tunnel junctions J with the source and the drain; it is capacitively coupled to the resonator biased by high dc voltage [9].

electrode was connected through a tunnel junction. The method had a 2.3×10^{-15} m $\mathrm{Hz}^{-1/2}$ threshold sensitivity to mechanical displacement, comparable with that of a single-electron transistor [2, 9], but a much narrower dynamic range.

2.4.4 Detection of NMR mechanical vibrations with the use of a single-electron transistor. The extremely high electric charge sensitivity of single-electron transistors makes them suitable for use as transducers of mechanical vibrations into an electrical signal, if a method to convert mechanical vibrations into variations of the electric charge is available. One way to do this is to capacitively couple an NMR to the island of a single-electron transistor (Fig. 8) and apply dc voltage V_{dc} to the NMR [9]. If the center of the NMR is displaced by x, there is a change in the charge induced on the island, $\Delta q = V_{\mathrm{dc}}\Delta C(x)$, where $\Delta C(x)$ is the change in capacitance between the gate and the island. Assuming that the gate and the island form a plane-parallel capacitor (as realized in a two-layer configuration [36]), we express the electrical charge variations due to mechanical displacement: $\Delta q \approx (x/d)C_0 V_{\mathrm{dc}}$, where C_0 is the equilibrium capacitance and d is the equilibrium distance between the gate and the island. At a given size of the structure, the efficiency of the transformation of a mechanical displacement into an electrical signal increases with V_{dc}. However, the dc voltage is limited by the breakdown voltage. The threshold sensitivity of the transistor to mechanical displacements depends on its noise characteristics. In an RF version of a transistor with a measured charge noise of $6 \times 10^{-6}\, e\, \mathrm{Hz}^{-1/2}$ [42], its threshold displacement sensitivity is $\delta x = 4 \times 10^{-6}$ Å $\mathrm{Hz}^{-1/2}$ at $d = 100$ nm, $C_0 = 5 \times 10^{-17}$ F, and $V_{\mathrm{dc}} = 5$ V. For comparison, the root-mean-square deviation from equilibrium due to zero-point vibrations of a 5 μm Al-based resonator of the thickness 39 nm, mass $m = 2.7 \times 10^{-16}$ kg, and resonant frequency $\omega_0/2\pi = 40$ MHz is $\sqrt{\hbar/(2m\omega_0)} \approx 7 \times 10^{-4}$ Å.

2.4.5 The optical method for studying NMR characteristics [43–45]. Optical detection is typically performed by means of optical interferometry. The method is based on the fact that a photon beam reflected from an NMR interferes with a test signal before it enters the photodetector. The analysis of the interference patterns allows restoring the NMR properties. However, the measurement sensitivity worsens as the size of the NMR decreases, because the diameter of the focused beam is limited from below by its diffraction properties. A possible solution could be the fabrication of waveguides of a submicron cross section located on the substrate near the NMR.

2.4.6 Measuring NMR displacements with a SQUID. The superconducting quantum interferometer device (SQUID) is the most sensitive magnetic flux detector [46]. Its dc sensor is a conducting loop with two Josephson junctions. At a given current flowing through the loop, the measured voltage is a function of the external magnetic flux. In other words, the sensor is sensitive to both the external magnetic field and the loop area. Therefore, a SQUID placed in a constant magnetic field can detect the vibrations of an NMR that is an integral part of the superconducting loop of its sensor. The first successful experiments toward this goal was recently reported in [47].

The SQUID threshold sensitivity to mechanical displacements can be estimated from the flux sensitivity $\delta\Phi \approx 10^{-6}\Phi_0\ \mathrm{Hz}^{-1/2}$ [46]. We regard the SQUID loop as a square with side L. Let one side form a resonator, i.e., be suspended above the substrate and capable of displacing parallel to its plane, thus changing the loop area. If a constant magnetic field B threads the loop, a displacement from the equilibrium position of the resonator by x changes the loop area by $(1/2)xL$, and therefore the flux by $\delta\Phi \approx (1/2)xLB$. Hence, the threshold sensitivity to mechanical displacement is $\delta x = 2\delta\Phi/(BL)$. This quantity is proportional to the constant magnetic field. If $B = 0.01$ T and $L = 1$ μm, $\delta x = 4 \times 10^{-7}$ Å $\mathrm{Hz}^{-1/2}$. Strong magnetic fields markedly suppress superconductivity of Al films; therefore, niobium structures can be used to enhance the threshold sensitivity (see [47]). Moreover, the threshold displacement sensitivity can be improved by using longer resonators at the expense of the resonance frequency. The threshold sensitivity determined by amplifier noises that has been experimentally achieved to date is around 10^{-4} Å $\mathrm{Hz}^{-1/2}$ for a 50 μm long resonator with a resonance frequency of 2 MHz [47].

2.4.7 Parameters of a modern NMRs. In Table 1, we list experimentally found values of the fundamental harmonic frequency and Q-factor of NMRs from metallic and nonmetallic materials. The second column shows temperatures at which measurements were made. The bottom line presents the

Table 1. Fundamental frequencies and Q-factors of certain NMRs.

Material of NMR	Temperature, K	Fundamental harmonic frequency f_0, MHz	Q	Reference
Si	4.2	70	2×10^4	[16]
Si	25	80	1.3×10^4	[17]
Si	20	25.598	3×10^4	[18]
SiC	4.2	198	1×10^3	[18]
SiC	20	71.91	4000	[19]
SiC	4.2	190 – 1029	500 – 5200	[20]
Pt	4	105.3	8500	[34]
Au	4	39	5000	[41]
Au	4.2	54.38	7510	[35]
Ti	4.2	194.47	3180	[35]
Al	4.2	180.86	5320	[35]
SiN	293	0.133	1.1×10^6	[48]

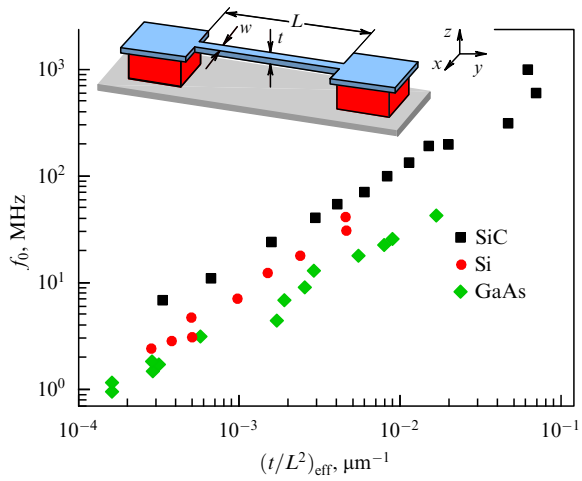

Figure 9. Dependence of the NMR fundamental harmonic frequency on the geometric parameter t/L^2, where t is the NMR thickness and L is the NMR length [1].

vibration data for a 50 nm thick SiN square membrane at $T = 293$ K [48].

The main problem currently facing NEMS developers is to achieve the highest possible first harmonic frequency without decreasing the Q value. From the standpoint of applications, the Q-factor determines the noise (fluctuation) bandwidth of a device, which is directly related to the NMR threshold sensitivity to the external signal being measured. Moreover, the Q-factor determines the maximum NMR-dissipated power.

Figure 9 taken from Ref. [1] shows a characteristic dependence of the fundamental harmonic frequency on the size of Si, SiC, and GaAs-based NMRs. Clearly, the highest frequency was obtained with a SiC NMR. The Q-factor decreases with increasing the frequency, the underlying cause being unknown. It may be either the losses from NMR interactions with the input and output transducers or the clamping losses between the NMR and the bulk material. Anyway, experiments with free–free NMRs allowed increasing their Q-factors more than two-fold [20].

Tables 2 and 3 present characteristics of SiC- and Al-based NMRs, showing that their Q decreases with increasing the resonance frequency.

Figure 10, borrowed from Ref. [20], shows the frequency dependence of Q for SiC NMRs fabricated by the same technology but differing in thickness (75, 80, and 100 nm). Their width ranged from 120 to 150 nm and the length was between 1 and 3 μm. The frequency was varied from 200 MHz to almost 1 GHz by changing the NMR length. The inset is a SAFM image showing the surface structure of an 80 nm thick SiC surface used to fabricate NMRs [20].

Table 2. Characteristics of SiC-based NMRs [20].

Resonant frequency, MHz	Length L, μm	Width w, nm	Thickness t, nm	NMR mass, fg	Q
190	2.35	150	100	145.0	5200
200	3.1	180	100	229.5	7500
241	1.8	150	100	111.1	1500
295	2.66	170	80	160.2	3000
339	1.6	140	75	71.3	3600
357	1.55	160	75	78.9	3000
395	1.75	129	80	74.4	2500
411	1.7	120	80	72.3	2500
420	1.8	150	100	111.1	1200
428	1.65	120	80	75.5	2300
480	1.32	140	75	61.3	1600
482	1.55	120	80	70.9	2000
488	1.31	150	75	60.8	1600
590	1.6	140	75	71.2	1700
712	1.55	160	75	78.9	900
1014	1.11	120	75	44.2	500
1029	1.09	120	75	43.4	500

Table 3. Characteristics of Al-based NMRs [35, 38].

Lwt, μm^3	$T = 4.2$ K		$T = 100$ mK	
	f_0, MHz	Q	f_0, MHz	Q
0.6 × 0.06 × 0.1			770	2400
1 × 0.06 × 0.1			360	30,000
1 × 0.1 × 0.2	544.93	1730		
2 × 0.1 × 0.2	180.86	5320	187	16,000
3 × 0.1 × 0.2	87.00	7140	110	41,000
5 × 0.1 × 0.2	39.44	9420	40.5	120,000

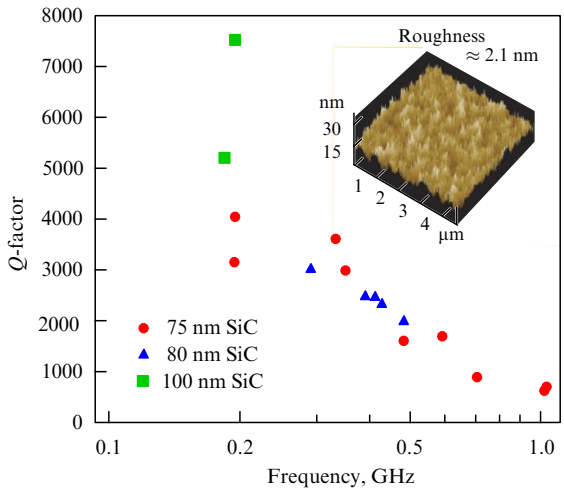

Figure 10. Dependence of Q on the fundamental harmonic frequency for several SiC NMRs clamped at both ends. The inset shows an image of the SiC surface obtained by scanning atomic force microscopy [20].

2.5 Power dissipated by nanomechanical resonators

The bandwidth of NMRs, as of any other resonator, can be written in the form $\Delta\omega = \omega_0/Q$. Then the power of thermal fluctuations at a temperature T is given by

$$P_{\min} \approx k_{\rm B} T \frac{\omega_0}{Q} \,. \tag{2.15}$$

The estimation of $P_{\min}$ for $T = 300$ K, $\omega_0/2\pi = 1$ GHz, and $Q = 10^4$ gives $P_{\min} \approx 2.6 \times 10^{-15}$ W. Increasing the last quantity by a factor of 10^4 for a reliable signal-to-noise ratio and assuming that one million such devices operate simultaneously on the chip, we obtain the dissipated power of the order of 10^{-5} W or almost five orders of magnitude smaller than the power dissipated in state-of-the-art all-electronic systems of the same level of complexity.

2.6 Intrinsic fluctuations of nanomechanical resonators

The damping of vibrations in an NMR and its Q are related to the energy exchange between NMR mechanical modes and other degrees of freedom, such as phonons, electrons,

bulk and surface defects of the resonator, and energy losses at the junctions between the resonator and the parent material.

The main source of intrinsic fluctuations in NMRs is thermomechanical fluctuations, which are analogous to Johnson–Nyquist noise in electrical circuits. In the classical limit, the spectral density of fluctuations of the nth harmonic can be written as [40]

$$S_{\mathrm{f}n}(\omega) = \frac{2k_{\mathrm{B}}Tm\omega}{\pi QL^2}\,, \qquad \omega \approx \Omega_n\,, \tag{2.16}$$

where T is the temperature, m is the resonator mass, L is its length, and Ω_n is the nth harmonic frequency defined by expression (2.7).

The quantity $\sqrt{S_{\mathrm{f}n}(\omega)}$ is the fluctuation force acting per unit length of the resonator in a unit frequency band. Therefore, the spectral density of fluctuations can be written in a form convenient for simple estimates:

$$S_x(\omega) = \frac{1}{(\omega^2-\omega_0^2)^2 + (\omega\omega_0/Q)^2}\,\frac{S_{\mathrm{f}n}(\omega)}{m^2}\,. \tag{2.17}$$

Amplitude fluctuations can also be written in the equivalent form of phase or frequency fluctuations that are often useful in concrete experiments. It should be borne in mind, however, that all these expressions are equivalent representations of the same amplitude fluctuations and describe no additional fluctuation sources.

For example, the spectral density of frequency fluctuations $S_\omega(\omega)$ can be expressed through the spectral density of thermomechanical amplitude fluctuations $S_x(\omega)$ as [40, 49]

$$S_\omega(\omega) = \left(\frac{\omega_0}{2Q}\right)^2 \frac{S_x(\omega)}{\langle x_0^2\rangle} \approx \frac{\omega_0^5}{Q^3}\,\frac{k_{\mathrm{B}}T}{E_{\max}}\,\frac{1}{(\omega^2-\omega_0^2)^2+\omega^2\omega_0^2/Q^2}\,, \tag{2.18}$$

where $\langle x_0^2\rangle$ is the maximum mean-square amplitude value and $E_{\max} = M_{\mathrm{eff}}\omega_0^2\langle x_0^2\rangle$ is the maximum fluctuation energy.

The fluctuation resonance width $\delta\omega_0$ is defined as

$$\delta\omega_0 \approx \left[\int_{\omega_0-\pi\Delta f}^{\omega_0+\pi\Delta f} S_\omega(\omega)\,\mathrm{d}\omega\right]^{1/2},$$

whence it follows that at $Q \gg 1$ and $2\pi\Delta f \ll \omega_0/Q$ (where Δf is the measurement frequency band),

$$\delta\omega_0 \approx \left[\frac{k_{\mathrm{B}}T}{E_{\max}}\,\frac{\omega_0\Delta f}{Q}\right]^{1/2}, \tag{2.19}$$

where we also used (2.18).

Another source of intrinsic fluctuations in NMRs is thermodynamic temperature fluctuations due to finite values of thermal conductivity and heat capacity. Because the heat capacity of NMRs is very low by virtue of its small size, this leads to relatively large temperature fluctuations, which in turn cause resonator frequency fluctuations, because the geometric dimensions and characteristics of the NMR material are temperature dependent.

The spectral density of temperature fluctuations can be written in the form [40]

$$S_T(\omega) = \frac{2}{\pi}\,\frac{k_{\mathrm{B}}T^2}{g}\,\frac{1}{1+\omega^2\tau_T^2}\,, \tag{2.20}$$

where g is the thermal conductivity and $\tau_T = c/g$ is the characteristic time needed for thermal equilibrium to set in (c is the heat capacity). As shown in [40], these fluctuations can be converted into resonance-frequency fluctuations of the resonator:

$$S_\Omega(\omega) = \left(\frac{1}{\Omega}\,\frac{\partial\Omega}{\partial T}\right)^2 S_T(\omega) = \left(-\frac{c_{\mathrm{s}}^2k_n^2}{\Omega_n^2}\,\alpha_T + \frac{2}{c_{\mathrm{s}}}\,\frac{\partial c_{\mathrm{s}}}{\partial T}\right)^2 S_T(\omega)\,, \tag{2.21}$$

where $c_{\mathrm{s}} = \sqrt{E/\rho}$ is the speed of sound in the material and α_T is the thermal expansion coefficient.

Other noise sources in NMRs include fluctuations associated with adsorption–desorption of residual gas molecules on the surface of NMRs and the noise produced by crystalline defects in the bulk of the resonator [1, 40, 49].

2.7 Detection of small masses

Ultrasensitive resonant mass detectors are applied in many branches of science and technology. Those with the highest sensitivity are based on the detection acoustic vibrations in crystals, thin films, and micrometer-scale cantilevers. All these devices operate by providing a shift of the sensor resonance frequency and a change in the Q-factor induced by an accreted particle whose mass is to be measured.

Due to the extremely small own mass of NMRs, they have a very high potential for detecting small masses; in principle, their sensitivity is sufficient to detect as small a mass as that of a single molecule [3, 49].

Mass detection by an NMR is based on measuring the resonance frequency shift upon accretion of a particle to the resonator. The change in the mass is related to frequency variations by the obvious formula

$$\delta M \approx \frac{\partial M_{\mathrm{eff}}}{\partial\omega_0}\,\delta\omega_0 = -2\,\frac{M_{\mathrm{eff}}}{\omega_0}\,\delta\omega_0\,, \tag{2.22}$$

where M_{eff} is the effective resonator mass, which for an NMR with a rectangular cross section can be written as $M_{\mathrm{eff}} = 0.735Ltw\rho$ [49], where L, t, and w are the geometric dimensions (see the inset in Fig. 9) and ρ is the density of the NMR material. The last expression after the equality sign in (2.22) follows from the relation $\omega_0 = \sqrt{k_{\mathrm{eff}}/M_{\mathrm{eff}}}$, where $k_{\mathrm{eff}} = 32Et^3w/L^3$ is the effective spring constant of the NMR.

The fundamental factor limiting the mass sensitivity threshold of an NMR is thermomechanical fluctuations giving rise to the resonance frequency instability.

For the threshold mass sensitivity, taking (2.19) into account, we have

$$\delta M \approx 2M_{\mathrm{eff}}\left(\frac{k_{\mathrm{B}}T}{E_{\max}}\right)^{1/2}\left(\frac{\Delta f}{\omega_0 Q}\right)^{1/2}. \tag{2.23}$$

Figure 11a [49] demonstrates the mass sensitivity of an NMR calculated by formula (2.23) and related to thermomechanical fluctuations. The value of δM is plotted in Daltons (Da) (1 Da = 1 a.m.u. = 1.66×10^{-24} g). It is calculated at the resonance frequency 1 GHz for two types of silicon NMRs with rectangular (solid line, $w\times t\times L = 50\times80\times780$ nm^3) and square (dashed line, $w\times t\times L = 15\times15\times340$ nm^3) cross sections.

Another source of errors in small-mass measurements is thermodynamic temperature fluctuations. In this case, the

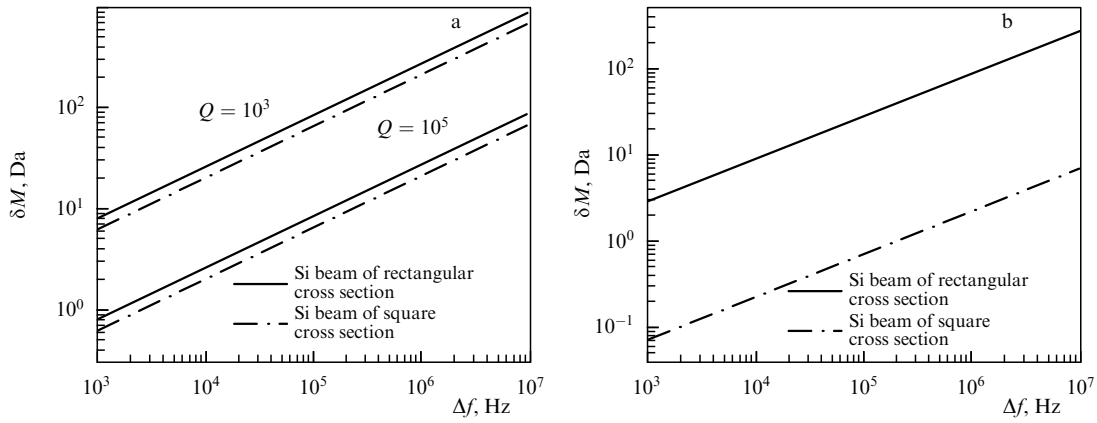

Figure 11. Dependence of the NMR mass sensitivity on the measurement frequency bandwidth due to (a) thermomechanical and (b) temperature fluctuations [49].

measurement error is given by [49]

$$\delta M \approx 2M_{\text{eff}} C \left(\frac{k_{\text{B}} T^2 \Delta f}{\pi g} \right)^{1/2}, \tag{2.24}$$

where the dimensional constant C depends on the physical properties of the NMR material. For a silicon bridge, $C = 1.26 \times 10^{-4}\ \text{K}^{-1}$ [49].

Figure 11b shows the dependence of the NMR mass sensitivity on the measurement frequency bandwidth attributable to thermodynamic temperature fluctuations and calculated from Eqn (2.24) [49]. The calculations were done for two types of NMR at $T = 300$ K and the same parameters as in Fig. 11a.

Two more sources of errors were analysed in Ref. [49]: adsorption/desorption of residual gas molecules at the NMR surface and elastic collisions of gas molecules with the surface. Taken together, all these sources of measurement errors give reason to conclude that the threshold mass sensitivity of NEMSs ranges from a few fractions to tens of Dalton, i.e., it is comparable with the mass of individual molecules. Such experiments are typically carried out [50] in a vacuum chamber where a flow of molecules is directed toward a resonator to which some of them adhere, thereby changing the resonance frequency. As mentioned above, this change can be measured in experiment.

In recent years, the threshold sensitivity of NEMSs as mass sensors has been annually improved by a factor of 10; today, it is close to 100 a.m.u., i.e., it remains inferior to the theoretical value of less than 1 a.m.u. [49, 51]. Table 4 shows the results of molecular mass measurements by NEMS obtained to date.

Studies of small-mass detection by NEMSs have shown that the smaller the resonator size at the minimal L/t ratio is, the better the results. As follows from Table 4, the best results were obtained using carbon nanotubes as the NMR [52–54]. The resonance frequency needs to be enhanced to 1 GHz at $Q \approx 10{,}000$ and the NMR mass of the order of 1×10^{-16} g if the threshold sensitivity equivalent to the single proton mass is to be achieved. This goal appears attainable in view of the advances in the modern technology of NMR fabrication.

Table 4. Results of molecular mass measurements by NEMS.

The smallest measured mass, a.m.u.	Frequency shift sensitivity $\delta f_0/\delta M$, Hz $(10^{-21}\ \text{g})^{-1}$	Resonance frequency f_0, MHz	NMR Q-factor	Reference
4.9×10^4	12	428		[50]
1.52×10^6	3×10^{-3}	32.8	3000	[3]
4.0×10^3	1	133 190	5000	[114]
15×10^3 (300 K) 840 (5 K)	11×10^3	143	50 (300 K) 865 (5 K)	[52]
200 (300 K)	0.104	328.5	1000 (300 K)	[53]
2.35×10^5		13.36	8500	[4]
50 (6 K)		300	200	[54]
1.8×10^9	0.01		10,000	[117]

2.8 Detection of ultrasmall displacements

Historically, studies on the detection of ultrasmall displacements started as searches for gravitational waves and the exploration of weak piezo- and magnetostriction effects and phase transitions in small-size samples at low temperatures [55–59]. The record high threshold sensitivity 6×10^{-9} Å Hz$^{-1/2}$ in the measurements with the use of an NMR displacement capacitive transducer at 40 kHz was achieved as early as 1981 [59]. It was subsequently improved to 2×10^{-9} Å Hz$^{-1/2}$ in laser interferometry measurements of fluctuations of a mechanical resonator placed in an optical cavity at 2 MHz [69].

However, such high threshold sensitivities are not necessarily inherent in nanoscale sensors. For example, the signal of a capacitive sensor can be indiscernible from the background noise generated by parasitic conductor capacitances coupling the sensor to the amplifier. Moreover, fiber-optic interferometers of extremely high (subangstrom) sensitivity cannot be used to study structures whose size is smaller than the optic fiber diameter. One of the methods having no geometric constraints is the magnetomotive method [16] described in Section 2.4.1. It was used to achieve a threshold sensitivity of the order of 3×10^{-5} Å Hz$^{-1/2}$ for a 1 MHz mechanical resonator [61].

In recent years, considerable progress has been made in the application of NEMSs for the detection of small displacements with a sensitivity close to the standard quantum limit (SQL). This goal was achieved using a variety of experimental methods, including registration of

Table 5. Results of displacement measurements by NEMS.

Displacement resolution, fm $Hz^{-1/2}$	Mean-square displacement (in SQL units)	Force resolution, aN $Hz^{-1/2}$	Temperature, mK	Type of transducer	Reference
2.3	42	78	250	Atomic point contact	[41]
200	30	3	200	Strip resonator	[60]
10	36 (133 fm)		20	dc-SQUID	[47]
2	100 (23 fm)		30	Single-electron transistor	[2]
3.8	4.3 (114 fm)		35	Single-electron transistor	[9]

NMR amplitude profiles by the atomic point contact technique [39], coupling of an NMR to a stripline resonator circuit [62], integration of a mechanical resonator into the loop of a superconducting quantum interferometer [47], and application of a single-electron transistor for recording NMR amplitude vibrations [2, 9]. The results of displacement measurements obtained thus far are presented in Table 5.

2.9 Application of carbon nanotubes and graphene as nanoelectromechanical devices

Carbon nanotubes (CNTs) provide an interesting alternative to traditional nanomechanical resonators [63]. These devices have attracted much attention since the publication of reports concerning multi-wall [64] and single-wall [65, 66] CNTs. Presently, they are among the most extensively studied NEMSs [67]. A single-wall CNT is a hollow graphene cylinder with one-carbon-atom thick walls. The tube can be several micrometers long and have a diameter of several nanometers. An ideal (defect-free) CNT can carry an electric current of the density 10^9 A cm^{-2} [68]. CNTs show either metallic or semiconducting properties, depending on the symmetry type. They are highly elastic (Young's modulus around 1 TPa [69]); hence, their resonant frequency is greater than 3 GHz [70]. Very soon after the discovery of CNTs, they began to be used as ultrasensitive nanomechanical sensors [71, 72]. Other proposed applications included mechanical structural elements of memory cells [73], relay structures [74], oscillators [75, 76], switches [77], and various types of sensors [78–80].

It is clear that the unique electrical and mechanical properties of CNTs make them promising candidates for use as ultrasensitive elements of NEMSs. The very small mass of CNTs (roughly 10^{-21} kg per μm length) results in the root-mean-square amplitude of zero-point vibrations of the order of 1 pm and enables their direct detection. Moreover, the small mass of CNTs make them highly sensitive mass [53, 54] and force [81] sensors.

Figure 12a schematically depicts a CNT-based device. The CNT is clamped between the ends of metalized pads functioning as tunnel junctions and coupled to the control gate (highly doped silicon) through a capacitance. CNT vibrations perpendicular to its axis change the capacitance between the CNT and the gate and thus alter the impedance of the measurement circuit.

The CNT vibration spectrum is far richer than that of metals or dielectric-based NMRs. Moreover, the peculiarities of interplay between CNT electrical and mechanical properties make it very difficult to measure CNT vibration modes [70].

Figure 12b is an SEM image of a CNT. CNT vibration modes are depicted in Fig. 12c. Figure 12d shows the dependence of the vibration mode energy on the CNT length. The radial breathing mode (RBM) shown in Fig. 12c (top) is inversely proportional to the CNT diameter d and does not depend on the CNT length L, whereas the transverse bending mode in Fig. 12c (bottom), inversely proportional to L^2, is a function of both the diameter and the stress. The two modes have a continuous frequency spectrum, shown as broadened bands in the upper and lower parts of Fig. 12d. The electron excitation energy E_e^* (upper curve in Fig. 12d) and the longitudinal stretching mode are inversely proportional to L. The experimental data points (squares in Fig. 12d for the stretching–compression mode shown in the middle part of Fig. 12c) correspond to the measured quantized vibrational modes [82].

A number of experiments with the use of various methods were performed to study bending vibration [83, 84] and radial breathing [85] modes for which the highest Q values were obtained. Table 6 presents the results of the measurement of the fundamental harmonic of CNT bending vibrations [70].

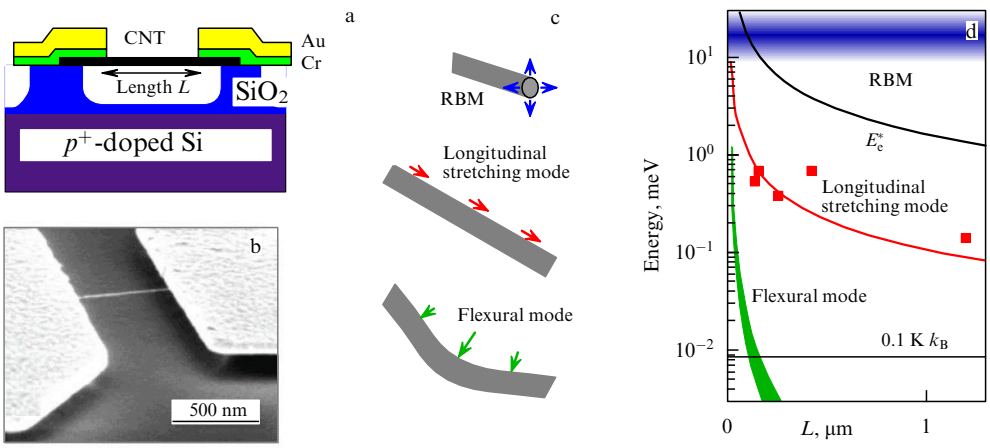

Figure 12. (a) Schematic representation of a CNT, (b) its scanning electron micrograph, (c) vibrational modes, and (d) vibration spectrum [82]. RBM (Radial Breathing Mode) vibrations of a CNT; E_e^* is the electron excitation energy.

Table 6. Experimental values of the fundamental harmonic of CNT bending vibrations [70].

Type of CNT	CNT length, nm	CNT radius, nm	Number of layers	Fundamental harmonic frequency, MHz
MW *	770	4.2	9	154
MW	1370	5	12	51
MW	650	5	12	264
MW	785	8	21	276
MW	195	5	12	2850
MW	265	10	27	3124
SW **	640	1.0		30
SW	465	0.6		260
SW	572	2.0		290
SW	193	0.7		573

* MW: multi-wall.
** SW: single-wall.

They show that the resonance frequency strongly depends on the CNT parameters. Resonance frequencies for a multi-wall CNT are more readily reproducible and better agree with the theory of an elastic beam clamped at both ends. Resonance quality factors in Ref. [70] are rather low (from 3 to 20), in contrast to those obtained earlier for a CNT of similar geometry. The quality factor of a CNT resonator in Refs [83, 86] ranges from 10 to 200. Recently developed mechanical resonators based on ultrapure CNTs have the frequency of the first harmonic amounting to hundreds of megahertz and the Q-factor higher than 10^5 [87]. Experiments with these CNT resonators revealed a strong coupling between mechanical vibrations and electron transport through a CNT [88, 89].

A recent study of the use of graphene as a material for NMRs [90] is worthy of mention. Such an NMR is schematically shown in Fig. 13. According to Ref. [90], it has $Q = 14{,}000$ at $T = 5$ K and the frequency 130 MHz. The threshold mass sensitivity measured at a signal integration time of 300 ms is around 2 zg, or significantly higher than that reported for nanotubes in Refs [53, 54]. It can be further improved by optimizing the noise characteristics of the readout electronics. Graphene resonators have more reproducible characteristics and a greater surface area than CNTs, which is important for small-mass detection. Graphene properties are highly susceptible to adsorbates, and this material can therefore be used in the future to create devices for the detection of individual molecules. Graphene has one more important, even if currently not well understood, property distinguishing it from other materials for NMR fabrication: high tensile breaking strength (130 ± 10) GPa at the limits strain of 0.25 [91]. This is crucial for the achievement of gigahertz frequencies while preserving the level of the signal being measured.

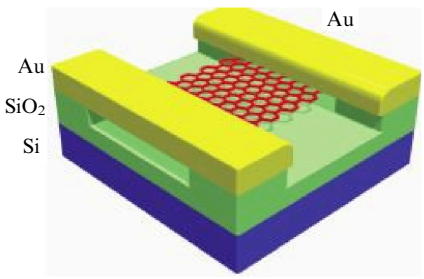

Figure 13. Schematic of a nanomechanical resonator made of a graphene sheet [90].

To conclude this section, we note that CNTs appear to be the most promising materials for designing NEMSs for a wide range of applications due to their small diameter and mass and the defect-free structure at the molecular level.

3. Applications of micro- and nanoscale cantilevers for the visualization of material structure

3.1 Introductory notes

The advent of scanning tunneling microscopy (STM) allowing the visualization of individual atoms [92, 93] (1982) was a truly revolutionary advance in surface physics. STM measures the tunneling current between the sample surface and the sensitive element (a micrometer-size tip) of the microscope. The operational principle of STM determines the range of its applications; specifically, it is suitable to study only conducting materials. This limitation motivated the development of atomic force microscopy (AFM) [94]; many researchers are currently focused on modifying it.

The principle of AFM operation is based on the measurement of forces acting between atoms of two bodies, the sample surface and the nanoscale cantilever clamped at one end above the surface. A change in the force resulting from the interaction between the sample and the tip of the cantilever causes the bending of the cantilever, detected by the methods described in Section 2. The magnitude of deflection carries information about both the surface topography and the interatomic interactions. Thus, while the cantilever in STM moves over the surface of constant tunneling current, the AFM cantilever moves over a constant force surface. The principles of feedback sensing even minor changes in the surface topography are practically identical in the two methods.

The threshold force sensitivity of modern AFM is $10^{-14} - 10^{-15}$ N, which is too low to detect a single-electron spin. Therefore, magnetic resonance force microscopy (MRFM) was developed [5, 44, 95–97] to improve the sensitivity of atomic force microscopy. MRFM differs from AFM in that it uses the cantilever mechanical properties.

The idea to detect nuclear magnetic resonance mechanically rather than inductively was suggested in 1991 [95]. In the framework of this approach, the fundamental mode of a mechanical resonator is related to the external force determined by the dynamics of the object under study. In practical devices, the silicon cantilever having a submicron ferromagnetic particle attached to its free end is excited by an alternating magnetic field at the frequency equal to its mechanical resonance frequency. The spin magnetic moment of the sample interacts with the cantilever and causes a shift in its vibration frequency. This idea was verified in 1994 in an experiment that for the first time demonstrated the possibility of mechanical detection of nuclear magnetic resonance of hydrogen nuclei in ammonium nitrate with the help of MRFM [44]. The threshold sensitivity achieved in the experiment amounted to 10^{13} spins in a 2.3 T field at room temperature, substantially higher than that of conventional inductive nuclear magnetic resonance imaging. In a later study, the method was used to measure the magnetic moment of a single-electron spin [98]. We note that the interaction

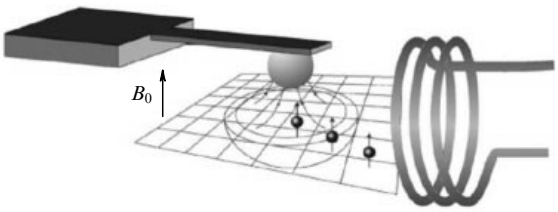

Figure 14. Schematic representation of the MRFM operation principle [100].

force between the nanocantilever and the electron spin in Ref. [98] was 10^{-18} N.

Today, MRFM provides a powerful tool for visualizing the surface of various materials [5, 99–102] with the 3D spatial resolution less than 10 nm [45], two orders of magnitude better than the resolution of conventional high-field magnetic resonance tomography. Moreover, the use of MRFM promoted considerable progress in nuclear spin detection [7, 44, 103–105].

The operating principle of MRFM is illustrated in Fig. 14. The free end of a cantilever is coated with a layer of ferromagnetic material that induces a strongly nonuniform magnetic field $B_1(r)$ in the sample material. Simultaneously, an external polarizing field B_0 is applied to the sample. As a result, the nuclear spins of the sample reside in the total nonuniform magnetic field

$$B(r) = B_0 + B_1(r)\,, \tag{3.1}$$

with the r-dependent nuclear magnetic resonance frequency $\omega(r) = \gamma B(r)$, where γ is the gyromagnetic ratio of the nuclei being studied. In addition, an RF magnetic field $B_{\rm rf}$ of the frequency $\omega_{\rm rf}$ close to the nuclear magnetic resonance frequency of nuclear spins at a concrete r value is applied to the sample by the coil depicted in the right part of Fig. 14. Thus, the alternating field acts only on those spins whose nuclear magnetic resonance frequency $\omega(r)$ coincides with $\omega_{\rm rf}$. Once the spatial configuration of the nonuniform magnetic field $B_1(r)$ is known, it is possible to reconstruct the spatial distribution of the nuclei of interest.

Figure 14 shows the mutual position of the cantilever and the sample as described in early studies. But it is not the only one possible. Its disadvantage ensues from the fact that if the cantilever lacks sufficient stiffness and is positioned close (a few hundred angstroms) to the surface, then the electrostatic forces and van der Waals forces may overcome the cantilever rigidity and cause its end to 'stick' to the sample surface. To avoid this, a different approach is frequently used (Fig. 15), in which the cantilever is positioned normally to the sample surface [106]. This highly rigid vertical construction excludes close contact of the cantilever with the sample, which can be kept spaced around 10 nm apart. Such a design also offers two variants. In one case, the magnetic material creating a magnetic field gradient is coated on the free end of the cantilever and the sample is placed directly underneath it (see Fig. 15). In the other, the free end of the cantilever is covered with the material to be examined while the magnetic material generating a nonuniform magnetic field is coated just under the cantilever.

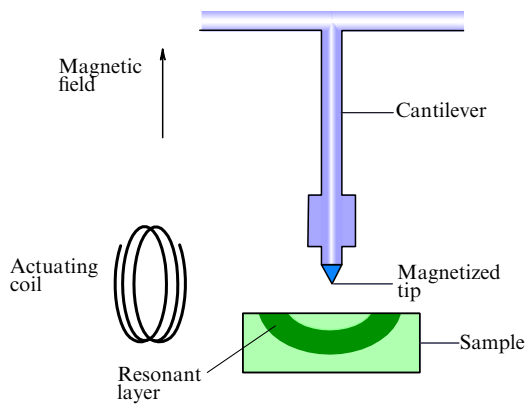

Figure 15. Vertically positioned cantilever with a magnetized tip affixed to its free end in the schematic diagram of a magnetic resonance force microscope.

3.2 Methods for signal detection in the magnetic resonance force microscopy

The equation for cantilever vibrations in the direction of a polarizing field B_0 (assumingly along the z axis) has the form

$$\frac{{\rm d}^2 z}{{\rm d}t^2} + \Gamma\,\frac{{\rm d}z}{{\rm d}t} + \omega_0^2 z = \frac{F_z}{m}\,, \tag{3.2}$$

where Γ is the resonator damping and

$$F_z = M_z\,\frac{{\rm d}B_z(\mathbf{r})}{{\rm d}z} \tag{3.3}$$

is the average force acting on the cantilever from all sample spins; M_z is the longitudinal component of nuclear spin magnetization depending on the polarizing (B_0), radiofrequency ($B_{\rm rf}$) fields, and nuclear relaxation times T_1 and T_2.

As the cantilever vibration amplitude is much smaller than the cantilever–sample distance, the magnetic field in (3.3) can be expanded up to the second order with respect to the small vibration amplitude:

$$B_z(\mathbf{r}) \approx B_z(\mathbf{r}_0) + \frac{{\rm d}B_z(\mathbf{r}_0)}{{\rm d}z}\,z + \frac{1}{2}\,\frac{{\rm d}^2 B_z(\mathbf{r}_0)}{{\rm d}z^2}\,z^2\,, \tag{3.4}$$

where r_0 is the distance between the cantilever and the spin in the stationary state.

With (3.3) and (3.4), the equation for cantilever vibrations (3.2) takes the form

$$\frac{{\rm d}^2 z}{{\rm d}t^2} + \Gamma\,\frac{{\rm d}z}{{\rm d}t} + \left(\omega_0^2 - \frac{M_z}{m}\,\frac{{\rm d}^2 B_z(\mathbf{r}_0)}{{\rm d}z^2}\right) z = \frac{M_z}{m}\,\frac{{\rm d}B_z(\mathbf{r}_0)}{{\rm d}z}\,. \tag{3.5}$$

It follows from Eqn (3.5) that interactions with the spins cause the cantilever resonance frequency to shift by

$$\Delta f = \frac{M_z f_0}{2k}\,\frac{{\rm d}^2 B_z(\mathbf{r}_0)}{{\rm d}z^2}\,, \tag{3.6}$$

where k is the cantilever spring constant.

Cantilever vibrations are excited not only by low-frequency (cantilever frequency) modulation of the external polarizing field B_0 but also by modulation of the RF excitation frequency $\omega_{\rm rf}$. This results in low-frequency oscillations of the spin magnetic moment M_z, which in turn induce low-frequency vibrations of the cantilever. We emphasize that MRFM detects low-frequency oscillations of the longitudinal magnetization component, whereas the conventional MRI technique measures high-frequency oscillations of the transverse component.

Table 7. Characteristics of certain MRF microscopes.

Parameters \ References	[109]	[110]	[107]	[98]
Mass, pg	3.9×10^4	6.4×10^3	2.0×10^3	92
Spring constant, mN m^{-1}	100	15	0.06	0.11
Frequency, Hz	8.0×10^3	7.7×10^3	850	5.5×10^3
Q-factor	2000	2.2×10^4	4.4×10^4	3.0×10^4
Magnetic field gradient, mT nm^{-1}	1.0×10^{-5}	0.25	0.028	0.20
Temperature, K	300	77	4	1
Amplitude sensitivity, pm Hz$^{-1/2}$	1	1	1	10
Force sensitivity, zN Hz$^{-1/2}$	4.1×10^6	2.4×10^5	7.8×10^3	6.7×10^3
Single-spin signal, zN	1.4×10^{-4}	3.5	0.39	2.8

Equation (3.5) implies two ways of detecting cantilever vibrations caused by nuclear spins. One is to directly detect the amplitude of these vibrations due to the spin force acting on the cantilever and described by the term in the right-hand side of Eqn (3.5). The amplitude of these vibrations (usually down to a few picometers) is detected by laser interferometry [103, 104]. The other method consists in measuring the cantilever resonant frequency shift given by Eqn (3.6) [107]. According to (3.6), this shift is proportional to the force gradient (usually of the order of a few millihertz).

3.3 Force and magnetic moment resolution of the magnetic resonance force microscope

The main factor limiting the MRFM sensitivity threshold is thermomechanical fluctuations of the cantilever, which are in most cases characterized by the white noise spectral density $S_f = 4k_B T m \Gamma$. These fluctuations lead to fluctuations of the cantilever vibration amplitudes at its resonance frequency ω_0 [99]:

$$\langle \Delta z^2 \rangle = \frac{4k_B T}{k\Gamma} \Delta f, \tag{3.7}$$

where k is the cantilever spring constant and Δf is the measurement frequency bandwidth, $\Gamma = \omega_0/Q$.

On the other hand, the cantilever vibration amplitude in resonance under the action of spin forces can be written as

$$\Delta z_f = \frac{\langle M_z \rangle |\nabla B|}{m\omega_0 \Gamma}. \tag{3.8}$$

A comparison of (3.7) and (3.8) yields the minimal magnetic moment that can be detected,

$$\langle M_z \rangle_{\min} = \frac{1}{|\nabla B|} \sqrt{\frac{4k_B T \Gamma k}{\omega_0^2} \Delta f} = \frac{1}{|\nabla B|} \sqrt{\frac{2k_B T k}{\pi Q f_0} \Delta f}. \tag{3.9}$$

Expression (3.9) can be rewritten using geometric and material parameters of the cantilever [106]:

$$\langle M_z \rangle_{\min} = \frac{1}{|\nabla B|} \left(\frac{wt^2}{LQ}\right)^{1/2} (E\rho)^{1/4} (k_B T \Delta f)^{1/2}. \tag{3.10}$$

The last expression can be represented in terms of the minimal detectable force [106]:

$$F_{\min} = \left(\frac{wt^2}{LQ}\right)^{1/2} (E\rho)^{1/4} (k_B T \Delta f)^{1/2}. \tag{3.11}$$

Table 7 lists characteristics of cantilevers, output threshold sensitivities of certain magnetic resonance force microscopes, and characteristics of MRFM-based devices used to detect nuclear spins. Higher threshold sensitivities were achieved in test measurements of cantilever noise and fluctuation parameters (e.g., when the cantilever was excited by an external force).

The most straightforward way to improve the threshold sensitivity is to decrease the cantilever stiffness and temperature. The fabrication technology of a 60 nm thick cantilever from single-crystal silicon with the spring factor $k = 6.5 \times 10^{-6}$ N m^{-1} is described in [69]. An MRF microscope with this cantilever had the force resolution 5.6×10^{-18} N Hz$^{-1/2}$ at $T = 4.8$ K, higher by a factor of 1000 than the typical value for AFM. A much higher sensitivity can be obtained using a rather stiff cantilever by decreasing the temperature. The achievement of the force resolution 8.2×10^{-19} N Hz$^{-1/2}$ using a cantilever with the spring constant $k = 260 \times 10^{-6}$ N m^{-1} at $T = 110$ mK was reported in [108].

The latest developments in this field have experimentally demonstrated the possibility of using MRFM in combination with reconstructive tomographic techniques for visualizing two-dimensional [7] and three-dimensional [45] spin density distribution with a high spatial resolution unattainable by conventional MRI. Because the spatial resolution is related to the magnetic field gradient G as $\Delta x = \Delta\omega/\gamma G$, where $\Delta\omega$ is the frequency resolution of the instrument, its high value was obtained by using a CoFe alloy to create the largest magnetic field gradient ever reached in experiments of this type: $G = 1.4 \times 10^6$ T m^{-1}. When constructing a two-dimensional image (the experiment in [7] to detect the magnetic moment of ^{19}F nuclei was carried out at $T = 0.6$ K), the spatial resolution proved to be around 100 nm, i.e., corresponded (with the known nuclei distribution density in the sample) to the sensitivity threshold of 1200 nuclear spins. Further improvement of this method permitted obtaining a 3D image of the proton density distribution in tobacco mosaic virus particles [45]. A spatial resolution of 10 nm was achieved, an almost 100 million-fold improvement over conventional MRI.

3.4 Detection of individual nuclear spins

The detection of individual nuclear spins is an important area of MRFM applications. There are no conceptual limitations on the use of MRFM for this purpose as a powerful tool to gain insight into the structure of biological molecules or, in a

broader sense, the structure of matter at the atomic and molecular levels. Moreover, MRFM is suitable for dynamic studies of the quantum evolution of individual spins during measurements, which is of great importance for the development of building blocks of quantum processors (qubits). Today, this goal seems to be only a distant dream, but it should be remembered that the sensitivity of MRFM for sensing spin magnetic moments has been increased by a factor of $10^6 - 10^7$ since 1992. In earlier experiments on the mechanical detection of electron spin resonance, the threshold magnetic moment sensitivity was only 1.5×10^{-17} J T^{-1} [109]. Later, it was improved to 1.7×10^{-21} J T^{-1} by significantly increasing the magnetic field gradient [110]. Presently, magnetic resonance force microscopy allows detecting electron spins with the sensitivity 9.3×10^{-24} J T^{-1} (which corresponds to the magnetic moment of a single electron) [98] and detecting nuclear spin resonance [7] with the sensitivity 1.6×10^{-23} J T^{-1} [a little more than 3000 detected particles (protons)].

3.5 Application of the nanomechanical cantilever as a biosensor

The unique sensitivity of nanocantilevers makes them highly attractive tools for biophysical and biochemical research. This section is focused on the main applications of nano- and microcantilevers as efficient chemical sensors and ultrasensitive biosensors. If a cantilever is treated with a chemical agent and placed in a proper medium, the resulting chemical reaction alters its mechanical properties, including mechanical stress, temperature, and mass. Such studies date back to 1994, when a cantilever was first used as a thermosensor for the registration of chemical reactions [111, 112].

A cantilever operates in three sensing modes: static, dynamic, and thermal.

The first is used to measure cantilever bending as a result of chemical or physical reactions on one of its surfaces previously covered with a layer of reactant. As the reactant adsorbs molecules from the environment, the cantilever bends down. In addition, electrostatic interactions between the reacting molecules at the cantilever surface cause longitudinal stress in its material [113]. A major drawback of the static mode is that the detected signal results from the collective action of many molecules. Moreover, it does not permit determining the number of molecules producing this signal. This problem can be resolved in the dynamic regime that allows estimating the number of molecules responsible for a change in the resonance frequency.

In the dynamic mode, it is possible to follow variations in the resonance frequency of the cantilever due to a change in its mass in the course of the chemical reaction at the surface. The best threshold mass sensitivity of a nanocantilever reported thus far amounts to a few zeptograms [114]. In 1995, the dynamic mode was first used to detect Hg vapors [115]. Ultrasensitive nanocantilevers developed later detect mass variations at the level of ≈ 1 ag [4] and ≈ 1 zg [114]. Other design variants of nanocantilevers were proposed for high-precision measurements of mass changes [1, 3, 116]. They enabled researchers to measure the mass of various viruses [117, 118]. Aluminum [119] and polymer [120] ultrasensitive cantilevers were tested (the latter were used to determine the mass of a deoxyribonucleic acid (DNA) molecule). As shown in Ref. [121], the threshold mass sensitivity of a cantilever can be further increased by operating it at higher vibration modes.

A cantilever operated in the thermal regime is covered on one side with a material having the thermal expansion coefficient different from that of the cantilever material. Silicon cantilevers are coated with gold, aluminum, or catalytically active platinum, whose thermal expansion coefficients are much higher than that of silicon. Changes in ambient temperature cause such cantilevers to bend; a deflection under the effect of a temperature change by a few microkelvins is readily detectable.

An interesting observation was made in Ref. [122], where a hollow cantilever was considered. The liquid of interest was passed through the hollow structure to alter its resonance characteristics. The threshold mass sensitivity achieved in [122] was 1 ag, sufficient to 'weigh' biomolecules and individual cells.

The first experiment on the use of a cantilever to study an exothermal chemical reaction with the energy about 1 pJ was carried out in the thermal regime in 1994 [111]. The thermal analysis of phase transitions with a small relaxation time (about 1 ms) was undertaken in Ref. [123]. The pH titration technique was used to unravel the relation between surface mechanical stress in the cantilever and the molecular structure of aqueous solutions of chemical agents. Changes in the mechanical stress of the order of 1.2 ± 0.3 mN m^{-1} detected at pH $= 6.0$ corresponded to the force of attraction between molecules equal to 1 pN [124]. Further developments in this field resulted in the creation of a so-called *artificial nose*, an array of cantilevers differing in functional characteristics; it was used to identify gaseous substances [125] and perfume constituents. Investigations of the artificial nose concept were continued in Refs [126, 127], where the frequency and amplitude of cantilever vibrations were measured simultaneously to characterize the physical and chemical properties of the ambient medium [126, 127].

A new line of genome research was initiated by experiments on the effect of DNA hybridization on the cantilever surface on its nanomechanical behavior [128]. Using this approach, a few femtomoles of DNA were detected in a solution containing 75 nanomoles of DNA [129]. The detection of RNA biomarkers at the picomol level that took only a few minutes was recently reported in Ref. [130].

Also, the possibility of using this method in proteomics was considered. Its clinical utility was demonstrated by the detection of prostate-specific antigen (PSA) in a broad concentration range, from 0.2 ng ml^{-1} to 60 μg ml^{-1}, for early diagnosis of prostate cancer [131]. The mechanical response of a cantilever to the alteration of the free energy of biomolecules on its surface provides a basis for the analysis of protein–protein and protein–nucleic-acid interactions, hybridization, and drug identification. Cantilever array-based sensors were used to simultaneously detect as many as 7 different antigen–antibody reactions, including additional thermomechanical and chemical reference points. It proved possible to continuously monitor two cardiac marker proteins, myoglobulin and creatine kinase, with the resolution up to 20 μg ml^{-1} [132]. Thinned cantilevers used to detect antigen molecules were shown to have an even better threshold sensitivity, of the order of 1 nmol [133].

The progress in DNA and protein detection technologies allowed an interesting experiment for the observation of protein–oligonucleotide interactions at the transcriptional level [134]. SP1 and NFkB transcription factors were detected independently in a solution containing 80 to 100 nmol of these molecules.

Conformational changes in biomolecules alter their mechanical properties and thereby mechanico-biological reactions. In one experiment, a cantilever coated with a monolayer of azobenzene molecules underwent periodic upward and downward bending as a result of interconversion of two configurations of molecules under the effect of periodic UV radiation [135].

The interaction of membrane proteins with their ligands results in conformational changes that carry information about intracellular processes. They were studied with the use of cantilevers in Refs [136–138].

Microcantilevers were also used to study nanomotion induced by controlled conformational changes in DNA molecules [139]. This motion causes a surface tension of 32 mN m^{-1}, corresponding to the force of an elementary molecular motor (11 pN m^{-1} or an order of magnitude lower than the values obtained earlier). Studies on the transformation of biochemical energy into micromechanical work open a new avenue for designers of mechanical nanobiosensors and micromachined devices.

Micromechanical oscillators were also used as fast-working biosensors to measure the growth rate of *Escherichia coli* bacteria [140, 141] and certain bacterial spores [142, 143]. The measurement was based on the changes in the cantilever resonance frequency upon an increase in its mass. The threshold sensitivity achieved in this study was 1000 *E. coli* cells per hour.

Paper [144] demonstrates the possibility of using microcantilevers for detecting explosives, exemplified by trinitrotoluene adsorbed on a cantilever surface covered with a layer of 4-mercaptobenzoic acid.

An important point to be made in conclusion is that nanocantilevers are beginning to be used for studying biological fluids. However, peculiarities of their functioning in liquid media impose specific requirements on the design of experiments [145]. Recent advances give hope of rapid progress in this area [146, 147].

4. Quantum properties of nanomechanical resonators

4.1 General remarks

The search for evidence of the quantum behavior of macroscopic mechanical objects is a long-term challenge facing theoretical physicists [56, 148, 149]. The solution of this problem depends on advances in solid-state nanotechnologies, giving reason to expect that the threshold sensitivity of nanomechanical resonators will be determined by the laws of quantum mechanics in the near future. As a rule, quantum mechanical constraints arise from Heisenberg's uncertainty principle, stating that any two observables whose operators do not commute cannot be measured simultaneously with arbitrary precision. The simplest example is the measurement of coordinate x and momentum p: $\Delta x \Delta p \geqslant \hbar/2$.

An NMR usually consists of $\sim 10^{10} - 10^{11}$ atoms. For such a 'macroscopic' (from the traditional quantum standpoint) body showing quantum properties, the boundary separating classical mechanics from quantum mechanics is appreciably shifted toward the former. We note that NMRs are not the sole macroscopic quantum object attracting attention of researchers. Superconducting charge [150] and flux [151] qubits created recently belong to the same family. The transition between the classical and quantum regimes of a flux qubit was observed in experiment [152]. We also note that electromagnetic oscillators, such as tank circuits [153, 154] or stripline resonators [155, 156], are frequently used for the measurement of superconducting qubits. This accounts for the current interest in the properties of oscillator–qubit and NMR–qubit systems.

4.2 Standard quantum limit of measurements

As is known, the accuracy with which a given quantity whose operator does not commute with the full Hamiltonian of the measurement system can be measured is *fundamentally* limited by the Heisenberg uncertainty relation. Such a limit is termed the standard quantum limit (SQL). For example, the accuracy of measurement of a quantum oscillator coordinate in amplitude/phase detection is defined by the expression [55]

$$(\Delta x)_{\mathrm{SQL}} = \sqrt{\frac{\hbar}{2m\omega_0}}\,, \tag{4.1}$$

coinciding with the fluctuation amplitude of its zero-point oscillations. In (4.1), m is the oscillator mass and ω_0 is its resonance frequency expressed, for example, for NMRs, through the spring constant k as $\omega_0^2 = k/m$.

Reaching the SQL in real experiments is essentially limited by the feedback effect of detector fluctuations on the NMR. Quantum mechanics imposes strict constraints on the minimal effect exerted by linear detector fluctuations on a test object [55, 56, 157, 158]. In the case of a continuous coordinate measurement and optimal matching between the linear detector and the object, the minimal attainable measuring accuracy is $\sqrt{2}$ times the SQL value in (4.1) [157]. This limitation is as fundamental as (4.1) because the detector 'coordinate' is assumed to be only linearly related to the oscillator coordinate.

Estimation of the measurement inaccuracy of NMR displacements at the SQL level is a difficult experimental problem. The SQL was most closely approached in schemes where single-electron transistors [2, 9, 159], SQUIDs [47], or quantum point contacts [41, 160] were used as NMR displacement transducers.

In principle, overcoming the standard quantum limit is possible using interferometric measurement systems based on counting the number of quanta or those where information about the oscillator displacement amplitude is contained in the interferometer signal phase [55, 161]. For NMRs, this means that information on the quantum state of a mechanical resonator can be obtained by detecting the quantum state of the related microwave field [162]. Considerable progress in this area proved feasible with the advent of a new generation of subquantum microwave amplifiers based on Josephson metamaterials [163]; their application allowed going 20% below the SQL [164]. Another approach is based on the interaction of an NMR with a silicon toroidal microwave resonator [165, 166]. This uses the interaction between the NMR and the microwave field of so-called whispering gallery modes in a toroidal resonator. In this case, the NMR is placed outside the toroid and its interaction with the microwave resonator occurs due to the penetration of the resonator microwave field through the toroid walls. Information about the displacement amplitude and fluctuations of the NMR is contained in the width of the resonance line and the frequency shift of the microwave field. With this system, the lowest measurement error reported thus far for NMR

displacements at room temperature (0.5 SQL) has been obtained [166]. The contribution of shot noise, which often dominates in such experiments, was much smaller, around 0.08 SQL.

It follows from (4.1) that the SQL depends on NMR properties, i.e., the greater the product $m\omega_0$ is, the lower the SQL. Substituting (4.1) in Eqn (2.9) for the fundamental harmonic frequency, we express the SQL in terms of the NMR parameters:

$$(\Delta x)_{\mathrm{SQL}} = \frac{0.389}{t}\sqrt{\frac{L}{w}}\sqrt{\frac{\hbar}{(E\rho)^{1/2}}}\,. \tag{4.2}$$

It follows from (4.2) for silicon ($E = 1.5\times 10^{11}$ N m^{-2}, $\rho = 2.33\times 10^3$ kg m^{-3}) that

$$(\Delta x)_{\mathrm{SQL}} = 2.36\times 10^{-5}\,\frac{1}{t}\sqrt{\frac{L}{w}}\ [\text{Å}]\,, \tag{4.3}$$

where the geometric parameters of the NMR are expressed in micrometers. For an NMR with dimensions $Ltw = 1\times 0.1\times 0.1$ μm^3, Eqn (4.3) gives $(\Delta x)_{\mathrm{SQL}} = 7.4\times 10^{-4}$ Å.

The above relations indicate that the fundamental frequency depends on the Young modulus E and density ρ as $\sqrt{E/\rho}$, while the coordinate uncertainty is defined by the SQL as $(E\rho)^{-1/4}$. This implies that for the SQL to be reached, maximally stiff (with a high Young modulus) and light (low-density) materials are to be used at a fixed mass. In this context, materials such as diamond, SiC, SiN, and AlN are preferred to Si and GaAs. Moreover, the quality factor of NMRs fabricated from these materials can in principle be increased (using their high chemical stability) by proper surface treatment. We also note that AlN shows good piezoelectric properties, which can be used to directly detect fluctuations of AIN-based NMRs [26, 167].

Although the value of the SQL for actually attainable NMR parameters m and ω_0 can be of the order of a few femtometers, the resonator position measurement error usually depends on the preamplifier noise. For example, at $m = 6.1\times 10^{-10}$ g and $\omega_0 = 2\pi\times 2$ MHz [47], $(\Delta x)_{\mathrm{SQL}} \approx$ 2.6 fm, even though the position measurement error in this experiment is $36(\Delta x)_{\mathrm{SQL}}$.

Despite multiple vibrational modes of NMRs, only a few fundamental ones actually interact with the detector. Given a very high quality factor of these modes, small vibrations of such a resonator are fairly well described by the model of a damped linear harmonic oscillator:

$$\frac{\mathrm{d}^2x}{\mathrm{d}t^2} + \Gamma\,\frac{\mathrm{d}x}{\mathrm{d}t} + \omega_0^2 x = \frac{F_{\mathrm{f}}(t)}{m}\,, \tag{4.4}$$

where Γ is the resonator damping, m is its mass, $\omega_0 = 2\pi f_0$ is the resonance frequency, and $F_{\mathrm{f}}(t)$ is the fluctuating force due to acoustic thermal oscillations of NMR atoms. The spectral density of these equilibrium fluctuations is defined by the fluctuation–dissipation theorem:

$$S_{\mathrm{f}}(\omega) = 2m\Gamma\hbar\omega\coth\frac{\hbar\omega}{2k_{\mathrm{B}}T}\,. \tag{4.5}$$

In the classical regime with $\hbar\omega \ll k_{\mathrm{B}}T$, Eqn (4.5) can be rewritten as $S_{\mathrm{f}}(\omega) = 4m\Gamma k_{\mathrm{B}}T$, whence the RMS value of the fluctuation force acting on the NMR is $F_{\mathrm{f}}^2 = 4m\Gamma k_{\mathrm{B}}T\Delta f$, where Δf is the measurement frequency bandwidth expressed in Hertz. It follows from (4.4) for the fluctuation displacement of the NMR equilibrium position in a unit bandwidth that

$$\delta x^2(\omega) = S_x(\omega)\,\frac{\mathrm{d}\omega}{2\pi} \equiv \frac{S_{\mathrm{f}}(\omega)}{m^2}\,\frac{1}{(\omega_0^2-\omega^2)^2+\omega^2\Gamma^2}\,\frac{\mathrm{d}\omega}{2\pi}\,, \tag{4.6}$$

where $S_x(\omega)$ is the spectral density of NMR displacement fluctuations. Assuming the NMR to be weakly damped ($\Gamma \ll \omega_0$), it is possible to integrate (4.6) over all frequencies, taking $S_{\mathrm{f}}(\omega)$ at the resonance point. In this way, the dispersion of NMR amplitude vibrations due to quantum fluctuations is found as

$$(\Delta x)^2 = \int_0^\infty S_x(\omega)\,\frac{\mathrm{d}\omega}{2\pi} = \frac{\hbar}{2m\omega_0}\coth\frac{\hbar\omega_0}{2k_{\mathrm{B}}T}\,. \tag{4.7}$$

Although Eqn (4.7) was obtained in the framework of the above approximations, it is exact and follows directly from quantum statistics in the computation of the mean potential energy of an undamped harmonic oscillator.

In actual practice, it is more convenient to use the spectral density of displacement fluctuations at the resonance frequency of a mechanical resonator. Equations (4.5) and (4.6) lead to

$$S_x(\omega_0) = \frac{S_{\mathrm{f}}(\omega_0)}{m^2\omega^2\Gamma^2} = \frac{2\hbar}{m\omega_0\Gamma}\coth\frac{\hbar\omega_0}{2k_{\mathrm{B}}T}\,, \tag{4.8}$$

where $S_x(\omega_0)$ is the unilateral spectral density in [m^2 Hz^{-1}] units. The first factor in the right-hand side of (4.8) is just the Fourier component of the SQL in (4.1) at the resonance frequency. For this reason, it is sometimes referred to as the standard quantum limit with respect to the spectral density of displacement fluctuations:

$$S_x^{\mathrm{SQL}}(\omega_0) = \frac{2\hbar}{m\omega_0\Gamma} = \frac{2\hbar Q}{m\omega_0^2}\,, \tag{4.9}$$

where $Q = \omega_0/\Gamma$ is the resonator quality factor.

Experimental Q-factors of low-lying NMR modes fall within the range 10^3-10^4, which enables the observation of quantum properties of such NMRs at appropriate temperatures.

Expressions (4.7) and (4.8) can be represented in the form

$$\Delta x = (\Delta x)_{\mathrm{SQL}}\sqrt{1+2N_{\mathrm{th}}}\,, \tag{4.10a}$$

$$S_x(\omega_0) = S_x^{\mathrm{SQL}}(\omega_0)\sqrt{1+2N_{\mathrm{th}}}\,, \tag{4.10b}$$

where N_{th} is the mean number of thermal phonons of the resonance mode ω_0 in the resonator:

$$N_{\mathrm{th}} = \frac{1}{\exp(\hbar\omega_0/k_{\mathrm{B}}T)-1}\,. \tag{4.11}$$

As follows from (4.10a) and (4.10b), the NMR vibration amplitude in thermodynamic equilibrium is bounded by the standard quantum limit and increases with temperature. The temperatures corresponding to $N_{\mathrm{th}} = 1$ (at which $\Delta x = \sqrt{3}\,(\Delta x)_{\mathrm{SQL}}$) are roughly equal to 9 mK at $\omega_0/2\pi =$ 100 MHz and 90 mK at $\omega_0/2\pi = 1$ GHz.

The resonator regime changes from classical to quantum when its thermal energy $k_{\mathrm{B}}T$ becomes comparable to the energy $\hbar\omega_0$ (or below) separating the resonator ground state from the first excited state:

$$\hbar\omega_0 \geqslant k_{\mathrm{B}}T\,. \tag{4.12}$$

In this case, the contribution of the thermal energy to the total vibrational mode energy is comparable to or lower than the zero-point vibration energy. The equality sign in Eqn (4.12) corresponds to $N_{\rm th} = 0.58$, while the temperature 1 K corresponds to the oscillator fundamental frequency equal to 21 GHz.

If $T > \hbar\omega_0/k_{\rm B}$, the number of thermal phonons can be roughly deduced from (4.11) as $N_{\rm th} \approx k_{\rm B}T/(\hbar\omega_0)$. However, there are no quantitative constrains on the value of $N_{\rm th}$ at which quantum properties begin to emerge. The smaller $N_{\rm th}$ is, the higher the probability of observing quantum effects in an NMR (entangled and squeezed states, pure superposition quantum states, zero-point vibrations). The condition $N_{\rm th} < 1$ is not always strictly necessary to enable the observation of quantum effects. Theoretical considerations suggest that quantum entanglement is in principle realizable at $T = 30$ mK and $f_0 = 50$ MHz [168]; at $N_{\rm th} \approx 50$, it is possible to form an NMR consisting of approximately 10^{10} atoms in a superposition of coordinate states [13]. In this sense, NMRs are radically different from gravitational wave detectors having a threshold displacement sensitivity of the order of several hundred SQLs [169–172]. However, the operating temperature of these detectors is relatively high (≈ 1 K), while the resonance frequencies are rather low (≈ 1 MHz); hence, $N_{\rm th} \approx 2 \times 10^4$. Recent progress in this field has allowed decreasing the fundamental mode temperature of a 2.7 kg mechanical pendulum to 1.4 μK with $N_{\rm th} \approx 200$ and the threshold sensitivity around 10 SQLs [173].

In contrast, NMR frequencies can be relatively high (a few GHz) [22, 167] with working temperatures 50–100 mK; in principle, this permits achieving $N_{\rm th} \ll 1$.

The lowest temperature currently attainable in dilution refrigerators is several millikelvins. The temperature of a sample coupled to the electronic components of the measurement circuit is somewhat higher (usually 20–50 mK), corresponding to radiofrequencies in the range 400–1000 MHz. Taking expression (2.9) for f_0 as a basis, we obtain

$$f_0 = 8.4\,\frac{t}{L^2}\ [\text{GHz}]\,, \tag{4.13}$$

for silicon ($E = 1.5 \times 10^{11}$ N m^{-2}, $\rho = 2.33 \times 10^3$ kg m^{-3}), where the resonator dimensions are given in micrometers. For the resonator 1 μm in length and 0.1 μm in width, from (4.13), $f_0 = 840$ MHz.

Thus, quantum effects of mechanical resonators can be observed if the resonators have submicron dimensions. Moreover, the lower the temperature to which NMRs can be cooled, the more stringent requirements are imposed on their dimensions at which quantum properties manifest themselves.

NMR quantum dynamics can be investigated directly using a highly sensitive displacement transducer. Currently, the most promising transducers for detecting zero-point fluctuations of NMRs are those recording one or more electrons in response to a change in the NMR position. These are tunnel devices [174–176], single-electron transistors [2, 9, 177–181], quantum dots [182], and quantum point contacts [183]. For example, using a single-electron transistor as a detector for NMRs with a frequency of 20 MHz, the authors arrived at a displacement resolution of the order of $4.3(\Delta x)_{\rm SQL}$ and the number of thermal photons $N_{\rm th} \approx 60$ [9, 179, 181]. Theoretical predictions [168] for the detection of NMR displacements based on a single-electron transistor suggest the possibility of achieving the threshold sensitivity up to 10^{-6} Å Hz$^{-1/2}$. For a resonator with the frequency 100 MHz and $Q = 10^4$, this estimate corresponds to a displacement resolution of the order of 10^{-4} Å. It can expected that the detection scenario proposed in Ref. [168] will allow reaching the level of zero-point fluctuations.

4.3 Dynamic cooling of nanomechanical resonators

It follows from Section 4.2 that investigations into the quantum behavior of nanomechanical oscillators are feasible under the condition that $\hbar\omega_0 \gg k_{\rm B}T$; in other words, their fundamental frequency must be as high as possible and the temperature as low as possible. Therefore, the main difficulty encountered in observations of quantum properties of macroscopic mechanical systems is posed by the necessity of cooling the mechanical mode to the ground-state temperature. For certain NMRs, such cooling is possible by purely technical means [167] often, either the required temperatures are lower than those attainable by standard cryogenic methods or the working temperatures are high due to the experimental design. Therefore, extensive efforts are devoted to the development of alternative cooling schemes based on ideas borrowed from quantum optics and methods for cooling atoms with laser light.

The majority of the methods for the dynamic cooling of a nanomechanical resonator use its interaction with an external system whose parameters vary with the NMR position. For optomechanical or electromenchanical systems, one such parameter is the resonance frequency of the optical or electric resonator coupled to the NMR. Leaving aside the details of concrete experimental setups, the equation for the NMR displacement amplitude can in most cases be written in the form

$$\frac{{\rm d}^2x}{{\rm d}t^2} + \Gamma_{\rm m}\,\frac{{\rm d}x}{{\rm d}t} + \omega_{\rm m}^2 x = \frac{F_{\rm f}(t)}{m} + \frac{1}{m}\int_0^t M\big(x(t')\big)\,h(t-t')\,{\rm d}t'\,, \tag{4.14}$$

where the functionals M and h depend on a given cooling method. The last term in the right-hand side of (4.14) leads to a renormalization of the intrinsic damping factor $\Gamma_{\rm m}$ and the resonance eigenfrequency $\omega_{\rm m}$ of NMRs, such that the root-mean-square magnitude of fluctuations, x, in the ${\rm d}\omega/(2\pi)$ bandwidth takes the form ($\hbar\omega_{\rm m} \ll k_{\rm B}T$)

$$\delta x^2(\omega) = \frac{4k_{\rm B}T\Gamma_{\rm m}}{m}\,\frac{1}{\big(\omega_{\rm eff}^2(\omega) - \omega^2\big)^2 + \omega^2\Gamma_{\rm eff}^2(\omega)}\,\frac{{\rm d}\omega}{2\pi}\,, \tag{4.15}$$

where $\Gamma_{\rm eff}$ and $\omega_{\rm eff}$ are functions of the frequency ω in general.

The effective temperature of the resonance mode of a nanooscillator is found from the equipartition theorem:

$$\frac{m\omega_{\rm m}^2\big\langle x^2(t)\big\rangle}{2} = \frac{k_{\rm B}T_{\rm eff}}{2}\,, \tag{4.16}$$

where $\big\langle x^2(t)\big\rangle$ is the result of the integration of expression (4.15) over all frequencies. Assuming that $\omega_{\rm eff} \approx \omega_{\rm m}$ and $\Gamma_{\rm eff} \ll \omega_{\rm m}$ in (4.15), we use (4.16) to obtain the effective temperature of the oscillator fundamental mode as [184]

$$T_{\rm eff} = T\,\frac{\omega_{\rm m}^2}{\omega_{\rm eff}^2(\omega_{\rm m})}\,\frac{\Gamma_{\rm m}}{\Gamma_{\rm eff}(\omega_{\rm m})}\,, \tag{4.17}$$

where $\Gamma_{\rm eff} = \Gamma_{\rm m} + \Gamma'$ with Γ' being the contribution to the damping of the mechanical resonator from its interaction with external devices. It follows from (4.17) that the effective

temperature is in general determined not only by damping but also by the resonance frequency shift. In this sense, an enhancement of resonator damping does not necessarily result in its cooling.

We emphasize that the above reasoning holds for the effective temperature of a *single mode* of the mechanical resonator that is kept at the thermodynamic temperature T as a whole.

A number of recent experiments have been performed to cool the fundamental mode of NMRs by coupling it to various external systems [162, 184–187]. These experiments showed that cooling to an effective temperature of 0.1 K [185] and even 5 mK is possible [186]. Ongoing theoretical studies are aimed at searching for more efficient cooling systems. The most promising of them is a combination of NMRs with a solid-state quantum electron device, such as an electrical resonator [188, 189], complanar multistrip line [15, 190], quantum dots [191], electron [192] and nuclear [193] spins, and superconductor devices [153, 159, 194–206].

4.4 Dynamic cooling in optomechanical systems

Realization of optomechanical systems in which optical and mechanical degrees of freedom are coupled by radiation pressure forces became possible due to technological advances in the fabrication of high-quality-factor optical microresonators and mechanical micro- and nanoresonators [187, 207–215].

Optomechanical systems, unlike those based on electromagnetic interactions of light with atoms, make it possible, theoretically, to realize strong coupling between the optical and mechanical modes. This fact attracts the attention of both theorists and experimentalists because it opens up new prospects for studying the quantum properties of light and macroscopic objects (in terms of quantum mechanics) with which it interacts.

A necessary and inevitable procedure is optomechanical cooling of the fundamental mode of a mechanical micro- or nanoresonator to ensure its transition to the ground state. In analogy with the laser cooling of atoms, the vibration mode energy of a mechanical oscillator decreases under the effect of the delayed radiation pressure force. However, in this system, cooling affects not a single atom but the collective vibrational mode of the macroscopic mechanical oscillator consisting of more than 10^{10} atoms.

The main component of an experimental setup is the Fabry–Perot resonator formed by two mirrors, one of which is fixed and the other is movable. The latter is usually a mechanical microbridge [210, 211]. The resonator is pumped by laser radiation, with the movable mirror being affected by a radiation pressure force proportional to the radiation energy density in the resonator. This force displaces the mirror, which results in a change in the resonator length and a resonance frequency shift with respect to the laser radiation frequency. The laser radiation, in turn, alters the radiation energy density and causes a change in the radiation force acting on the micromirror. Such coordinated dynamics of optical radiation and mechanical bridge vibrations account for many interesting effects in the system under consideration. These effects have been investigated in many mechanical systems in the context of dynamic cooling of the fundamental mode of nano- and microelectromechanical systems [159, 184, 185, 187, 210, 211], improvement of sensitivity of gravitational wave detectors [216, 217], and generation of squeezed photon states [218].

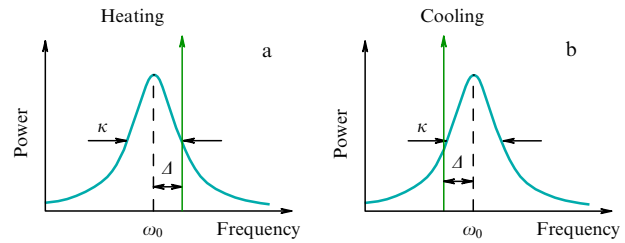

Figure16. Resonance characteristic of the optical density.

The key factor determining the dynamics of a mechanical resonator under the effect of the radiation pressure force is a somewhat delayed (rather than instantaneous) change in response to a change in the resonator position. The delay is the time needed for a photon to leak out of the optical resonator; it is proportional to the resonator quality factor. For this reason, the dependence of the radiation force on the mechanical resonator displacement is a usual Lorentzian whose peak position coincides with the resonance frequency of the optical cavity.

We assume that the laser frequency is on the left slope of the resonance curve (detuning Δ) of the optical cavity, as shown in Fig. 16b. Oscillations of the movable mirror then cause the working point to move up and down on the slope of the resonance curve. When the photon lifetime in the cavity $\tau_\kappa \approx 1/\kappa$ (where κ is the width of the cavity resonance curve) is much shorter than the period of mechanical oscillations ($\omega_{\rm m} \ll \kappa$), the radiation pressure force changes almost instantaneously upon a change in the resonator position. In other words, in this adiabatic case, changes in the radiation force and the resonator position occur virtually in-phase. Therefore, the net work of the radiation force during a single oscillation period of the resonator is close to zero and there is no energy transfer between the cavity and the resonator. If the mechanical oscillation period is slightly longer than the photon lifetime in the cavity ($\omega_{\rm m} \leqslant \kappa$), the radiation force approaching the resonance is weaker than the equilibrium one due to the time lag, but is greater far from the resonance. As a result, the total work of the radiation force for one oscillation period of the mechanical resonator is negative, which implies energy transfer from phonons to the cavity photons and cooling of the resonator oscillation mode.

When the laser frequency corresponds to the right slope of the resonance curve (the detuning Δ in Fig. 16a), radiation pressure has the opposite effect, that is, the total work of the radiation force during a single oscillation period of the resonator is positive, which implies heating of the resonator oscillation mode. This action of the radiation force on a mechanical resonator was first described some 40 years ago, based on the interaction between a resonator and a high-Q electrical loop [219–221]. In the modern literature, it is referred to as dynamical backaction, because the light field affects the mechanical resonator *after* being excited by this resonator.

The semiclassical analysis of this effect leads to an expression analogous to (4.17) for the effective temperature of the vibrational mode,

$$T_{\rm eff} = T\,\frac{\Gamma_{\rm m}}{\Gamma_{\rm m} + \Gamma_{\rm opt}}\,, \tag{4.18}$$

where the optomechanical friction $\Gamma_{\rm opt}$ depends linearly on the laser power and is highly sensitive to the displacement of the mechanical resonator. Therefore, cooling is a consequence of the delayed response of the radiation force to a change in the thermal fluctuation amplitude of the mechanical resonator. This delay is due to a finite leakage rate κ of photons leaving the resonator cavity.

A detailed quantum analysis [222, 223] has demonstrated that expression (4.18) is valid if $\Gamma_{\rm opt} \ll \kappa$, $\Gamma_{\rm m}/(\Gamma_{\rm m} + \Gamma_{\rm opt}) > 1/Q_{\rm m}$, and the number of thermal phonons is relatively large ($N_{\rm th} = k_{\rm B}T/(\hbar\omega_{\rm m}) \gg 1$). Despite the nonequilibrium state of the oscillation mode cooled to $T_{\rm eff}$, it is possible, by analogy with (4.11) and assuming the mechanical oscillator to be weakly damped ($\Gamma_{\rm m} \ll \Gamma_{\rm opt} \ll \kappa$), to introduce the mean number of its phonons

$$n_{\rm opt} = \frac{1}{\exp\left[\hbar\omega_{\rm m}/(k_{\rm B}T_{\rm eff})\right] - 1}\,.$$

The total number of phonons of a mechanical oscillator is found from the balance of absorbed and emitted energies [223]:

$$n_{\rm m} = \frac{\Gamma_{\rm opt} n_{\rm opt} + \Gamma_{\rm m} N_{\rm th}}{\Gamma_{\rm m} + \Gamma_{\rm opt}}\,, \tag{4.19}$$

where $N_{\rm th}$ is the number of thermal phonons corresponding to the temperature $T_{\rm m}$, and $\Gamma_{\rm opt}$ and $n_{\rm opt}$ are determined by the interplay between mechanical and optical resonators. At $N_{\rm th} \gg 1$, Eqn (4.19) reduces to classical expression (4.18).

The lowest attainable temperature depends on quantum field fluctuations in the optical resonator, which leads in the resolved sideband limit ($\omega_{\rm m} \gg \kappa$) at $\Delta = -\omega_{\rm m}$ (where $\Delta = \omega_{\rm las} - \omega_{\rm cav}$ is the laser frequency detuning of $\omega_{\rm las}$ from the cavity resonant frequency $\omega_{\rm cav}$) to the minimally attainable average number of 'optical' phonons in the mechanical resonator [222–224]:

$$n_{\rm opt} = \left(\frac{\kappa}{4\omega_{\rm m}}\right)^2 \ll 1\,. \tag{4.20}$$

As follows from (4.19) and (4.20), cooling to ground-state temperatures is quite possible in the limit $\omega_{\rm m} \gg \kappa$ and $\Gamma_{\rm opt} \gg \Gamma_{\rm m}$. However, this level has not yet been reached in experiments. The minimal number of thermal phonons obtained thus far is roughly 30 in Ref. [225] and 60 in Ref. [226].

Apart from the standard realization of the optomechanical system described above, in which one of the micromirrors of the optical Fabry–Perot resonator serves as a mechanical resonator, other optomechanical systems were investigated that are based on a similar operating principle, with radiation pressure forces playing the key role. Cantilevers [184, 185] and microbridges [210, 211] were used as mechanical resonators having typical masses $10^{-15} - 10^{-10}$ kg (and even 1 g [212]) and typical frequencies in the range 1 kHz–100 MHz.

The coupling of optical and mechanical modes via radiation pressure is possible using not only a Fabry–Perot resonator but also other optical resonators in which whispering gallery modes (WGMs) are realized [227], such as microtoroids [187, 207, 209, 228–232], microspheres [233, 234], and microdisks [235].

Radiation pressure in WGM resonators is directed normally to the beam path [207–209], whereas in Fabry–Perot devices, the momentum transfer between optical and mechanical modes occurs in the direction of light propagation. The coupling between optical and mechanical oscillations is due to radiation pressure on the walls of the WGM resonator undergoing numerous internal reflections during light circulation, leading to its radial mechanical vibrations.

One more type of optomechanical system proposed in Ref. [236] has recently been investigated both theoretically [237–240] and experimentally [213, 241]. The role of the mechanical element in such systems is played by a dielectric membrane placed between the fixed mirrors of a Fabry–Perot resonator, such that radiation pressure acts on either side of the mechanical resonator. In the experiment described in Ref. [213], the room temperature of the fundamental mode of the mechanical oscillator was lowered to 6.8 mK, roughly corresponding to 1100 thermal quanta. An advantage of this method is the possibility, in principle, of positioning the mechanical membrane strictly in an antinode of a standing wave. The radiated power is therefore sensitive to the squared membrane displacement amplitude $\langle x^2 \rangle$, which enables direct detection of the mechanical oscillator energy by the 'quantum nondemolition' method.

4.5 Cooling of nanoelectromechanical systems

The use of NEMSs for the investigation of quantum properties of mechanical oscillators has certain advantages over the application of optomechanical systems, all the more because the currently available technologies make it possible to build solid-state structures containing a nanomechanical resonator and an electronic circuit on a chip.

The idea of controlling oscillations of the fundamental mode of a mechanical oscillator via an electrical circuit is by no means new [219, 220]. In NEMSs based on this principle, the mechanical oscillator is one of the plates of a capacitor forming part of the tank circuit whose resonance frequency and amplitude depend parametrically on the oscillation amplitude of the mechanical resonator. At the given parameters of the electrical circuit, the regime of oscillations of the mechanical resonator depends on the frequency and power of external pumping and varies in a broad range, from the strong-damping stable one to the unstable regenerative regime.

The main results pertaining to this scheme can be derived from an analysis of the diagram in Fig. 17 based on the same principle as an optomechanical scheme. Here, the role of radiation pressure is played by the Coulomb force between the plates of a mechanical capacitor. Oscillations of a

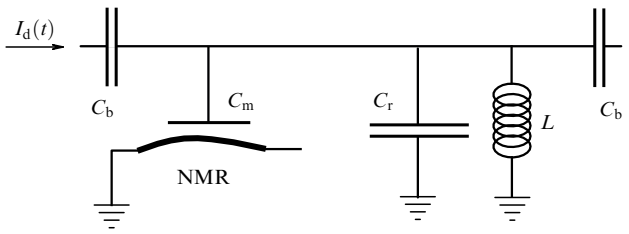

Figure 17. A nanoelectromechanical system consisting of an NMR connected to a microstrip resonator: $I_{\rm d}$ is the excitation current, $C_{\rm b}$ is the capacitance coupling the external measurement circuit to the microwave resonator, $C_{\rm r}$ is the capacitance of the microstrip resonator, L is the resonator inductance, and $C_{\rm m}$ is the capacitance of the mechanical resonator.

mechanical resonator modulate the capacitance of the mechanical capacitor, leading to a modulation of the resonance frequency ω_0 of the entire circuit. If the excitation frequency $\omega_{\rm rf}$ is tuned to the left slope of the resonance curve ($\omega_0 > \omega_{\rm rf}$), the modulation of ω_0 results in charge modulation on the mechanical capacitor, which leads to a change in the Coulomb force acting on the mechanical oscillator. However, variations of the force do not coincide in phase with changes in the oscillation amplitude of the mechanical oscillator owing to the finite relaxation time of the electrical circuit. If $\omega_0 > \omega_{\rm rf}$, the phase shift causes the force to be directed against the oscillator velocity, thereby damping its oscillations. This effect generally leads to a shift in the oscillator resonance frequency and a change in the damping coefficient.

This scenario was thoroughly considered in Ref. [56] with respect to gravitational-wave experiments. The first experiments on the dynamic cooling of gravitational detectors were undertaken over 15 years ago using a mechanical oscillator in the form of a 1300 kg niobium plate with an eigenfrequency of 700 Hz [169]. The plate was part of a superconducting RF cavity having an eigenfrequency of 10 GHz modulated by niobium plate vibrations. Excitation of the RF cavity at a frequency close to its resonance suppressed mechanical oscillations of the fundamental mode of the niobium detector from the initial level corresponding to the temperature of the whole setup (5 K) to the level corresponding to $T = 2$ mK ($N_{\rm th} \approx 6 \times 10^3$). The advantages of this approach have recently been demonstrated in Ref. [189], where a rather big mechanical oscillator (length 1.5 mm, fundamental frequency 7 kHz) was cooled from room temperature to $T = 45$ K with the use of an LC-tank circuit with a resonance frequency of 100 MHz.

In what follows, we briefly discuss the problems related to the application of this system in nanomechanics. Coupled electrical and mechanical resonators can be described by two differential equations:

$$\ddot{x} + \Gamma_{\rm m}\dot{x} + \omega_{\rm m}^2 x = -\frac{q_{\rm m}^2}{2mC_{\rm m}^0 d} + \frac{F_{\rm f}(t)}{m} \tag{4.21}$$

for the mechanical resonator and

$$\ddot{q} + \Gamma_{\rm r}\dot{q} + \omega_{\rm r}^2(x)q = \frac{1}{L}\left(V_{\rm f}(t) + V_{\rm rf}\cos\omega t\right) \tag{4.22}$$

for the electrical one.

In Eqn (4.21), x is the displacement of the mechanical resonator from the equilibrium position; m, $\Gamma_{\rm m}$, and $\omega_{\rm m}$ are the mass, damping, and eigenfrequency of the mechanical oscillator; $q_{\rm m}$ is the charge of the 'mechanical' capacitor; and $C_{\rm m}^0$ and d are its static capacitance and interplate distance. The first term in the right-hand side of Eqn (4.21) is the Coulomb force acting on one mechanical plate from the other; the minus sign in front of it reflects the fact that the Coulomb force is always attractive. The quantity $F_{\rm f}(t)$ in the right-hand side of (4.21) is the fluctuation force acting on the mechanical oscillator; the spectral density of its equilibrium fluctuations is given by expression (4.5). In Eqn (4.22), $\Gamma_{\rm r}$ and $\omega_{\rm r}$ are the damping and resonance frequency of the electrical component $\omega_{\rm r}(x) = 1/\sqrt{L(C_0 + C_{\rm m}(x))}$, where C_0 is the equilibrium capacitance of the capacitor, $C_{\rm m}(x)$ is the mechanical capacitance depending on the interplate distance $d + x$, and q is the total charge on the capacitors related to $q_{\rm m}$ as

$$q_{\rm m} = \frac{C_{\rm m}(x)}{C_0 + C_{\rm m}(x)}\, q\,.$$

The quantity $V_{\rm f}(t)$ in the right-hand side of (4.22) is the noise voltage in the electrical circuit and $V_{\rm rf}$ is the external signal amplitude. The interaction between mechanical and electrical systems is determined by the dimensionless parameter $\varepsilon = C_{\rm m}^0/C_0$. Equations (4.21) and (4.22) admit an analytic solution in the case of small mechanical oscillations ($x \ll d$) and relatively slow vibrations of the mechanical resonator compared with electrical ones ($\omega_{\rm m} \ll \omega_{\rm r}$). At $\Gamma_{\rm r} \ll \omega_{\rm m}$, external signal pumping at the side frequency $\omega \approx \omega_{\rm r} - \omega_{\rm m}$ can significantly suppress the resonance mode fluctuations of the mechanical oscillator. Then the expression for the effective temperature of the fundamental mode of the mechanical oscillator takes the form

$$T_{\rm eff} = T_{\rm m}\,\frac{\Gamma_{\rm m}}{\Gamma_{\rm eff}}\left(1 + \eta\varepsilon^2\,\frac{T_{\rm r}}{T_{\rm m}}\,\frac{\omega_{\rm r}^2}{\omega_{\rm m}^2}\right), \tag{4.23}$$

where

$$\Gamma_{\rm eff} = \Gamma_{\rm m}\left(1 + \eta\varepsilon^2\,\frac{\omega_{\rm r}^3}{\omega_{\rm m}^3}\right), \tag{4.24}$$

$$\eta = \frac{P_{\rm rf}}{32md^2\Gamma_{\rm r}\Gamma_{\rm m}}\,, \tag{4.25}$$

and $T_{\rm r}$ is the thermodynamic temperature of the electrical part of the system, which can in theory be different from the thermodynamic temperature $T_{\rm m}$ of the mechanical oscillator.

The second term in the right-hand side of Eqn (4.23) is the contribution of thermal fluctuations of the electrical part resulting from the nonlinear coupling between mechanical and electrical systems. These fluctuations limit the effective temperature of the mechanical resonator maximally attainable in side-band cooling. The contribution of this term becomes dominant if the power input $P_{\rm rf}$ is enhanced. In this case, it follows from (4.23) for the attainable limit of the effective temperature [198] that

$$T_{\rm eff}^{\rm min} = T_{\rm r}\,\frac{\omega_{\rm m}}{\omega_{\rm r}}\,. \tag{4.26}$$

Condition (4.26) is important specifically for NEMSs, because the frequency ratio $\omega_{\rm m}/\omega_{\rm r}$ in NEMSs is much higher than in optomechanical schemes. The quantum analysis of this problem [198] also leads to relation (4.26). It follows from (4.26) that the starting temperature of a microwave resonator must correspond to its ground-state temperature if the oscillator is to be cooled to the ground state $T_{\rm eff}^{\rm min} < T_{\rm m}^* \leqslant \hbar\omega_{\rm m}/2k_{\rm B}$. In other words, the microwave resonator must be originally 'cooler', i.e., have fewer thermal photons, than the mechanical one.

Good prospects for the application of the above cooling setup for the transition of mechanical nano- and microoscillators into the quantum mode have been demonstrated in a number of recent studies [61, 162, 164, 242–244]. The authors used a superconducting microstrip resonator as the electronic component coupled to a mechanical oscillator, with the circuit parameters satisfying conditions for the most efficient cooling (resolved side-band cooling), $\Gamma_{\rm r} \ll \omega_{\rm m}$, in which the excitation frequency of the microstrip resonator matches the side frequency $\omega = \omega_{\rm r} - \omega_{\rm m}$. Paper [244] for the first time

Table 8. Cooling of micromechanical resonators in optomechanical systems.

Mechanical resonator parameters				Initial ambient temperature, K	Effective fundamental mode temperature, K	Root-mean-square displacement sensitivity, m $Hz^{-1/2}$	Reference
Effective mass m, g; material	Length × width × thickness, μm	Fundamental mode frequency f_m, MHz	Q factor				
190×10^{-6} Si	$10^3 \times 10^3 \times 60$	0.814	10,000	300	2	4×10^{-19}	[210]
400×10^{-9} TiO_2/SiO_2	$520 \times 120 \times 2.4$	0.28	10,000	300	8	8×10^{-13}	[211]
1.0×10^{-8} Si	Microtoroid	73.5	30,000	300	20	5×10^{-19}	[214]
Si	$120 \times 3 \times 0.1$	0.0039	55,600	2.2	0.290	1.0×10^{-12}	[186]
3.8×10^{-9} Au/Si	$223 \times 22 \times 0.46$	0.0073		300	18	1.0×10^{-11}	[184]
2.4×10^{-8}	$450 \times 50 \times 2$	0.0125	20,000	300	0.135	1.0×10^{-13}	[185]
4×10^{-8} SiN	$10^3 \times 10^3 \times 0.05$	0.134	1.1×10^6	294	6.82×10^{-3}	7×10^{-16}	[213]
43×10^{-9} SiN	$100 \times 50 \times 1$	0.945	30,000	5.3	0.0015	2.6×10^{-17}	[225]
125×10^{-9} Si	$50-300 \times 50 \times 5.4$	0.557	1000 – 3000	295	17		[215]
40×10^{-9} Si	$50-300 \times 50 \times 5.4$	0.557	1000 – 3000	35	0.29		
1.5×10^{-8}	Microtoroid	58	2890	300	11	2.5×10^{-18}	[187]
4.1×10^{-8} Si	Microtoroid, $d = 30$ μm	118.6	3400	1.4	0.21	1.5×10^{-18}	[234]
1		172×10^{-6}	3200	300	0.8	5×10^{-16}	[212]
4.9×10^{-12} SiN	$35 \times 0.8 \times 0.11$	8	40,000	300		5.7×10^{-16} (0.7 SQL)	[165]
30×10^{-6} Si	Microtoroid, $d_{min} = 6$, $d_{max} = 60$, thickness 10	6.272		300	58	1.5×10^{-18}	[232]
$(1-10) \times 10^{-9}$ Si	Microtoroid	62 – 122	2600	1.65	0.125	1.5×10^{-18}	[226]
20×10^{-9} Si	Microtoroid	70	5000	0.6	0.037	3.2×10^{-19}	[231]

demonstrated purely quantum nondemolition measurements of mechanical oscillator vibrations. The idea behind this well-known method [55, 148] is to measure one of the quadrature components, X_1 or X_2 ($x(t) = X_1 \cos(\omega_m t) + X_2 \sin(\omega_m t)$), rather than the quantity x, which is not an integral of motion for the oscillator. Although the components X_1 and X_2 do not commute with each other, either of them is an integral of motion; in other words, they are dynamically decoupled. For this reason, the measurement, e.g., of the X_1 component has no effect on its evolution, even if it affects X_2 (owing to their noncommutativity). In Ref. [244], this idea was realized by simultaneous excitation of a microwave resonator by two phase-coherent signals at frequencies $\omega_{red} = \omega_r - \omega_m$ and $\omega_{blue} = \omega_r + \omega_m$. The field in this microwave resonator was modulated at the resonance frequency of the mechanical oscillator $E(t) = E_0 \cos(\omega_r t) \cos(\omega_m t)$, while the filtered signal amplitude was proportional to X_1.

The dynamic cooling of an NMR was demonstrated in a setup of a different type, where a superconducting single-electron transistor was used as the displacement transducer [159]. The authors used the backaction of electrical shot noise to cool the mechanical oscillator. They managed to reduce the temperature of a nanomechanical oscillator with a frequency of 21.9 MHz from 550 mK to 300 mK, which corresponds to $N_{th} = 25$.

On-chip solid-state NEMSs are very convenient to integrate into low-temperature modules of modern cryogenic equipment. Purely cryogenic NEMS cooling has yielded excellent results. A threshold sensitivity close to the SQL was demonstrated with the use of single-electron transistors [2, 9, 159], SQUIDs [47], and quantum point contacts [41, 160] as NMR displacement transducers. In this context, we note a recent study [167] in which an NMR with a frequency of 6.175 GHz was cooled to $T = 25$ mK, corresponding to $N_{th} \ll 1$. The NMR was fabricated from aluminum nitride (strong piezoelectric) and its oscillations were directly converted into electrical signals detected by a superconducting phase qubit. The number of thermal

Table 9. Cooling of NMRs in electromechanical systems.

Mechanical resonator parameters				Initial ambient temperature, K	Effective fundamental mode temperature, K	Root-mean-square displacement sensitivity, m $Hz^{-1/2}$ (coordinate resolution un units of SQL)	Reference
Effective mass m, g; material	Length × width × thickness (Lwt), μm	Fundamental mode frequency f_m, MHz	Q factor				
2×10^{-12} Al	$50 \times 0.1 \times 0.3$	1.41	3800	0.2	0.14		[242]
2×10^{-12} Al	$50 \times 0.13 \times 0.1$	0.237	2300	0.04	0.002	1.6×10^{-12}	[60]
6.2×10^{-12} Al	$100 \times 0.13 \times 0.12$	1.525	3×10^5	0.05	0.01	5.5×10^{-14}	[162]
Si	$1500 \times 200 \times 14$	0.007	20,000	300	45		[189]
SiN – Al	$30 \times 0.17 \times 0.14$	6.3	10^6	0.146	0.0013	1.125×10^{-15}	[243]
2.2×10^{-12} SiN	$30 \times 0.17 \times 0.06$	5.57	2.5×10^5	0.142	0.013	(1.3)	[244]
11×10^{-12} Al	$150 \times 0.17 \times 0.16$	1.04		0.015		4.8×10^{-15} (0.8)	[164]
AlN		6175	260	0.025	0.025		[167]
Al/SiN	9×0.2	21.9	150,000	0.3	0.15	3.8×10^{-16} (3.9)	[159]
9.7×10^{-13} Au/SiN	$8 \times 0.2 \times 0.1$	19.7	35,000	0.056	0.056	3.8×10^{-15} (4.3)	[9]
2.84×10^{-12} GaAs	$3 \times 0.25 \times 0.2$	116	1700	0.03	0.03	2×10^{-15} (100)	[2]
6.1×10^{-10} Nb	$L = 50$	2	18,000	0.02	0.084	1×10^{-14} (36)	[47]
2.3×10^{-12} Au	$5.6 \times 0.22 \times 0.1$	43.1	5000	5	5.73	2.3×10^{-15} (42)	[41]
2×10^{-9} Si	$350 \times 3 \times 1$	5.2×10^{-3}	2500	4.2	4.2	1×10^{-12}	[160]
GaAs	$L = 50$, $t = 0.72$	1.5	3000	4.2	4.2	3×10^{-12}	[183]

phonons in the NMR did not exceed 0.07. It was concluded that direct cryogenic cooling allowed the NMR to be obtained in the ground state.

The main experimental data on the dynamic cooling of optomechanical and nanoelectromechanical systems are listed in Tables 8 and 9. The first column of both tables presents effective mass values of mechanical resonators determined either from the known spring constant and the measured resonance frequency or from the amplitude response of the resonator to the applied external force. Some cells in the tables are left blank due to the lack of relevant data in the cited publications.

5. Conclusions

We have focused on the analysis of the development of nanoelectrochemical systems during the past decade. The principal physical and material characteristics and properties of nanomechanical resonators, as well as their applications in fundamental and experimental studies, have been reviewed. We anticipate the development of these investigations in the near future along the following three major lines.

One is the further improvement of fabrication technologies for silicon and metallic NMRs with the aim to achieve fundamental frequencies of a few tens of gigahertz to enable an insight into the quantum behavior of NMRs at the moderately low temperatures ($\gtrsim 100$ mK) attainable in many laboratories. A different way to address this problem is to develop methods for the dynamic cooling of nanoresonators in order to significantly decrease the effective temperature of the fundamental mode. There is much theoretical research along these lines, but none of the proposed techniques to switch over a nanomechanical resonator to the quantum regime, i.e., to obtain $N_{th} \ll 1$, have yet been realized in experiment.

The second line is the use of NMRs as biosensors. Extensive studies in this area are currently underway based on micrometer resonators. There is little doubt that transition to submicrometer resonators will open up new prospects for the application of NMRs as ultrasensitive biosensors.

Developments along the third line have a very short history of only 3 or 4 years. They are focused on the use of CNTs and graphene as nanomechanical resonators. There are still many unexplored topics in this field that, nonetheless, appear very promising, because it is expected to promote research on the relation between CNT quantum and mechanical properties and thereby create opportunities for designing and producing new measuring devices.

Many laboratories worldwide are currently engaged in NMR research. The ever-increasing interest in NMRs is

primarily due to seeking solutions to basic problems related to the quantum behavior of macroscopic objects and quantum measurements. Furthermore, the interest in NMRs is stimulated by the prospects of their practical application. High resonance frequencies and quality factors of these devices, coupled to the ease of their integration into electrical and optical systems, provide a solid basis on which to develop ultrasensitive detectors for the measurement of many physical quantities at the level of their quantum fluctuations. There is no doubt that investigations into the quantum properties of NMRs will result in the development of new types of detectors and related electronics.

Acknowledgments

We are grateful to O Astafiev, A G Vostretsov, L B Ioffe, D A Knyazev, Yu G Peisakhovich, O S Fedorova, A A Shtygashev, L Faoro, M Grajcar, F Hoehne, H Im, T F Li, Y Nakamura, J P Pekola, and J S Tsai for the useful discussions of certain problems considered in the paper.

The work was supported by the Russian Ministry of Education and Science in the framework of federal target programs (GK 02.740.11.5067, GK 14.740.11.0061, GK 14.740.11.0828, GK 16.552.11.7036, P798), the German Ministry of Science (BMBF), RUS 10/015 project, MEXT Grant-in-Aid 'Quantum Cybernetics', and JSPS through the FIRST program.

References

1. Ekinci K L, Roukes M L *Rev. Sci. Instrum.* **76** 061101 (2005)
2. Knobel R G, Cleland A N *Nature* **424** 291 (2003)
3. Ekinci K L, Huang X M H, Roukes M L *Appl. Phys. Lett.* **84** 4469 (2004)
4. Ilic B et al. *J. Appl. Phys.* **95** 3694 (2004)
5. Sidles J A et al. *Rev. Mod. Phys.* **67** 249 (1995)
6. Cleland A N, Roukes M L *Nature* **392** 160 (1998)
7. Mamin H J et al. *Nature Nanotechnol.* **2** 301 (2007)
8. Roukes M L, in *Technical Digest of the 2000 Solid State Sensor and Actuator Workshop* (Cleveland, OH: Transducers Research Foundation, 2000); cond-mat/0008187
9. LaHaye M D et al. *Science* **304** 74 (2004)
10. Nishiguchi N *Phys. Rev. B* **68** 121305(R) (2003)
11. Buks E et al. *Europhys. Lett.* **81** 10001 (2008)
12. Blencowe M P, Buks E *Phys. Rev. B* **76** 014511 (2007)
13. Armour A D, Blencowe M P, Schwab K C *Phys. Rev. Lett.* **88** 148301 (2002)
14. Wang Y-D, Semba K, Yamaguchi H *New J. Phys.* **10** 043015 (2008)
15. Xue F et al. *Phys. Rev. B* **76** 205302 (2007)
16. Cleland A N, Roukes M L *Appl. Phys. Lett.* **69** 2653 (1996)
17. Feng X L et al. *Nano Lett.* **7** 1953 (2007)
18. Ekinci K L et al. *Appl. Phys. Lett.* **81** 2253 (2002)
19. Yang Y T et al. *Appl. Phys. Lett.* **78** 162 (2001)
20. Huang X M H et al. *New J. Phys.* **7** 247 (2005)
21. Carr D W et al. *Appl. Phys. Lett.* **75** 920 (1999)
22. Huang X M H et al. *Nature* **421** 496 (2003)
23. Beck R G et al. *Appl. Phys. Lett.* **73** 1149 (1998)
24. Tang H X et al. *Appl. Phys. Lett.* **81** 3879 (2002)
25. Sekaric L et al. *Sensors Actuators A* **101** 215 (2002)
26. Cleland A N, Pophristic M, Ferguson I *Appl. Phys. Lett.* **79** 2070 (2001)
27. Sekaric L et al. *Appl. Phys. Lett.* **81** 4455 (2002)
28. Hutchinson A B et al. *Appl. Phys. Lett.* **84** 972 (2004)
29. Postma H W Ch et al. *Appl. Phys. Lett.* **86** 223105 (2005)
30. Cleland A N *Foundations of Nanomechanics* (Heidelberg: Springer, 2002)
31. Li H et al. *J. Appl. Phys.* **100** 094309 (2006)
32. Imboden M et al. *Appl. Phys. Lett.* **90** 173502 (2007)
33. Gaidarzhy A et al. *Appl. Phys. Lett.* **91** 203503 (2007)
34. Husain A et al. *Appl. Phys. Lett.* **83** 1240 (2003)
35. Li T F et al. *Appl. Phys. Lett.* **92** 043112 (2008)
36. Pashkin Yu A et al. *Appl. Phys. Lett.* **96** 263513 (2010)
37. Greywall D S et al. *Phys. Rev. Lett.* **72** 2992 (1994)
38. Hoehne F et al. *Phys. Rev. B* **81** 184112 (2010)
39. Flowers-Jacobs N E, Schmidt D R, Lehnert K W *Phys. Rev. Lett.* **98** 096804 (2007)
40. Cleland A N, Roukes M L *J. Appl. Phys.* **92** 2758 (2002)
41. Truitt P A et al. *Nano Lett.* **7** 120 (2007)
42. Aassime A et al. *Phys. Rev. Lett.* **86** 3376 (2001)
43. Rugar D, Mamin H J, Guethner P *Appl. Phys. Lett.* **55** 2588 (1989)
44. Rugar D et al. *Science* **264** 1560 (1994)
45. Degen C L et al. *Proc. Natl. Acad. Sci. USA* **106** 1313 (2009)
46. Clarke J, Braginski A I (Eds) *The SQUID Handbook* Vol. 1 (Weinheim: Wiley-VCH, 2004)
47. Etaki S et al. *Nature Phys.* **4** 785 (2008)
48. Zwickl B M et al. *Appl. Phys. Lett.* **92** 103125 (2008)
49. Ekinci K L, Yang Y T, Roukes M L *J. Appl. Phys.* **95** 2682 (2004)
50. Naik A K et al. *Nature Nanotechnol.* **4** 445 (2009)
51. Cleland A N *New J. Phys.* **7** 235 (2005)
52. Lassagne B et al. *Nano Lett.* **8** 3735 (2008)
53. Jensen K, Kim K, Zettl A *Nature Nanotechnol.* **3** 533 (2008)
54. Chiu H-Y et al. *Nano Lett.* **8** 4342 (2008)
55. Caves C M et al. *Rev. Mod. Phys.* **52** 341 (1980)
56. Braginsky V B, Khalili F Ya *Quantum Measurement* (Cambridge: Cambridge Univ. Press, 1995)
57. Shmal'gauzen V I *Usp. Fiz. Nauk* **132** 679 (1980) [*Sov. Phys. Usp.* **23** 858 (1980)]
58. Andronik K I, Pudalov V M *Pis'ma Zh. Eksp. Teor. Fiz.* **35** 157 (1982) [*JETP Lett.* **35** 192 (1982)]
59. Braginskii V B, Panov V I, Popel'nyuk V D *Pis'ma Zh. Eksp. Teor. Fiz.* **33** 423 (1981) [*JETP Lett.* **33** 405 (1981)]
60. Hadjar Y et al. *Europhys. Lett.* **47** 545 (1999)
61. Mohanty P, Harrington D A, Roukes M L *Physica B* **284** 2143 (2000)
62. Regal C A, Teufel J D, Lehnert K W *Nature Phys.* **4** 555 (2008)
63. Hierold C et al. *Sensors Actuators A* **136** 51 (2007)
64. Iijima S *Nature* **354** 56 (1991)
65. Ijima S, Ichihashi T *Nature* **363** 603 (1993)
66. Bethune D S et al. *Nature* **363** 605 (1993)
67. Dresselhaus M S, Dresselhaus G, Avouris P (Eds) *Carbon Nanotubes: Synthesis, Structure, Properties, and Applications* (Berlin: Springer, 2001) p. 391
68. Bhushan B (Ed.) *Springer Handbook of Nanotechnology* (Heidelberg: Springer, 2004)
69. Zhang P et al. *Int. J. Solids Struct.* **39** 3893 (2002)
70. Garcia-Sanchez D et al. *Phys. Rev. Lett.* **99** 085501 (2007)
71. Williams P A et al. *Appl. Phys. Lett.* **82** 805 (2003)
72. Fennimore A M et al. *Nature* **424** 408 (2003)
73. Rueckes T et al. *Science* **289** 94 (2000)
74. Lee S W et al. *Nano Lett.* **4** 2027 (2004)
75. Nishio M et al. *Appl. Phys. Lett.* **86** 133111 (2005)
76. Papadakis S J et al. *Phys. Rev. Lett.* **93** 146101 (2004)
77. Cha S N et al. *Appl. Phys. Lett.* **86** 083105 (2005)
78. Stampfer C et al. *Nano Lett.* **6** 233 (2006)
79. Dharap P et al. *Nanotechnology* **15** 379 (2004)
80. Grow R J et al. *Appl. Phys. Lett.* **86** 93104 (2005)
81. Poncharal P et al. *Science* **283** 1513 (1999)
82. Hüttel A K et al. *New J. Phys.* **10** 095003 (2008)
83. Sazonova V et al. *Nature* **431** 284 (2004)
84. Reulet B et al. *Phys. Rev. Lett.* **85** 2829 (2000)
85. LeRoy B J et al. *Nature* **432** 371 (2004)
86. Witkamp B, Poot M, van der Zant H S J *Nano Lett.* **6** 2904 (2006)
87. Hüttel A K et al. *Nano Lett.* **9** 2547 (2009)
88. Steele G A et al. *Science* **325** 1103 (2009)
89. Lassagne B et al. *Science* **325** 1107 (2009)
90. Chen C et al. *Nature Nanotechol.* **4** 861 (2009)
91. Lee C et al. *Science* **321** 385 (2008)
92. Binnig G et al. *Appl. Phys. Lett.* **40** 178 (1982)
93. Binnig G et al. *Phys. Rev. Lett.* **50** 120 (1983)
94. Binnig G, Quate C F, Gerber Ch *Phys. Rev. Lett.* **56** 930 (1986)
95. Sidles J A *Appl. Phys. Lett.* **58** 2854 (1991)
96. Sidles J A *Phys. Rev. Lett.* **68** 1124 (1992)
97. Züger O et al. *J. Appl. Phys.* **79** 1881 (1996)
98. Rugar D et al. *Nature* **430** 329 (2004)
99. Suter A *Prog. Nucl. Magn. Res. Spectrosc.* **45** 239 (2004)
100. Kuehn S, Hickman S A, Marohn J A *J. Chem. Phys.* **128** 052208 (2008)
101. Hammel P C, Pelekhov D V, in *Handbook of Magnetism and Advanced Magnetic Materials* Vol. 5 *Spintronics and Magnetoelectronics* (Eds-in-Chief H Kronmüller, S Park) (Hoboken, NJ: John Wiley & Sons, 2007)

102. Hammel P C et al. *Proc. IEEE* **91** 789 (2003)
103. Thurber K R, Harrel L E, Smith D D *J. Magn. Res.* **162** 336 (2003)
104. Thurber K R et al. *Appl. Phys. Lett.* **80** 1794 (2002)
105. Mamin H J et al. *Phys. Rev. B* **72** 024413 (2005)
106. Stowe T D et al. *Appl. Phys. Lett.* **71** 288 (1997)
107. Garner S R et al. *Appl. Phys. Lett.* **84** 5091 (2004)
108. Mamin H J, Rugar D *Appl. Phys. Lett.* **79** 3358 (2001)
109. Rugar D, Yannoni C S, Sidles J A *Nature* **360** 563 (1992)
110. Bruland K J et al. *Appl. Phys. Lett.* **73** 3159 (1998)
111. Gimzewski J K et al. *Chem. Phys. Lett.* **217** 589 (1994)
112. Thundat T et al. *Appl. Phys. Lett.* **64** 2894 (1994)
113. Wu G et al. *Proc. Natl. Acad. Sci. USA* **98** 1560 (2001)
114. Yang Y T et al. *Nano Lett.* **6** 583 (2006)
115. Wachter E A, Thundat T *Rev. Sci. Instrum.* **66** 3662 (1995)
116. Craighead H G *Science* **290** 1532 (2000)
117. Ilic B, Yang Y, Craighead H G *Appl. Phys. Lett.* **85** 2604 (2004)
118. Gupta A, Akin D, Bashir R *Appl. Phys. Lett.* **84** 1976 (2004)
119. Davis Z J, Boisen A *Appl. Phys. Lett.* **87** 013102 (2005)
120. Calleja M et al. *Ultramicroscopy* **105** 215 (2005)
121. Dohn S et al. *Appl. Phys. Lett.* **86** 233501 (2005)
122. Burg T P et al. *Nature* **446** 1066 (2007)
123. Berger R et al. *Appl. Phys. Lett.* **69** 40 (1996)
124. Watari M et al. *J. Am. Chem. Soc.* **129** 601 (2007)
125. Lang H P et al. *Appl. Phys. A* **66** 2532 (1998)
126. Baller M K et al. *Ultramicroscopy* **82** 1 (2000)
127. Battiston F M et al. *Sensors Actuators B* **77** 122 (2001)
128. Fritz J et al. *Science* **288** 316 (2000)
129. McKendry R et al. *Proc. Natl. Acad. Sci. USA* **99** 9783 (2002)
130. Zhang J et al. *Nature Nanotechnol.* **1** 214 (2006)
131. Wu G et al. *Nature Biotechnol.* **19** 856 (2001)
132. Arntz Y et al. *Nanotechnology* **14** 86 (2003)
133. Backmann N et al. *Proc. Natl. Acad. Sci. USA* **102** 14587 (2005)
134. Huber F et al. *Biosens. Bioelectron.* **21** 1599 (2006)
135. Ji H-F et al. *Chem. Commun.* (22) 2532 (2004)
136. Zhang Y et al. *Biosens. Bioelectron.* **19** 1473 (2004)
137. Braun T et al. *Biophys. J.* **90** 2970 (2006)
138. Mukhopadhyay R et al. *Nano Lett.* **5** 2385 (2005)
139. Shu W et al. *J. Am. Chem. Soc.* **127** 17054 (2005)
140. Gfeller K Y, Nugaeva N, Hegner M *Biosens. Bioelectron.* **21** 528 (2005)
141. Gfeller K Y, Nugaeva N, Hegner M *Appl. Environ. Microbiol.* **71** 2626 (2005)
142. Nugaeva N et al. *Biosens. Bioelectron.* **21** 849 (2005)
143. Nugaeva N et al. *Microscopy Microanalysis* **13** 13 (2007)
144. Pinnaduwage L A et al. *Langmuir* **19** 7841 (2003)
145. Braun T et al. *Phys. Rev. E* **72** 031907 (2005)
146. Dorrestijn M, Doctoral Dissertation (Basel: Institute for Physics, Univ. of Basel, 2006)
147. Dorrestijn M et al. *Phys. Rev. Lett.* **98** 026102 (2007)
148. Bocko M F, Onofrio R *Rev. Mod. Phys.* **68** 755 (1996)
149. Cho A *Science* **299** 36 (2003)
150. Nakamura Y, Pashkin Yu A, Tsai J S *Nature* **398** 786 (1999)
151. van der Wal C H et al. *Science* **290** 773 (2000)
152. Grajcar M, Izmalkov A, Il'ichev E *Phys. Rev. B* **71** 144501 (2005)
153. Il'ichev E et al. *Phys. Rev. Lett.* **91** 097906 (2003)
154. Born D et al. *Phys. Rev. B* **70** 180501(R) (2004)
155. Wallraff A et al. *Nature* **431** 162 (2004)
156. Oelsner G et al. *Phys. Rev. B* **81** 172505 (2010)
157. Caves C M *Phys. Rev. D* **26** 1817 (1982)
158. Clerk A A *Phys. Rev. B* **70** 245306 (2004)
159. Naik A et al. *Nature* **443** 193 (2006)
160. Poggio M et al. *Nature Phys.* **4** 635 (2008)
161. Caves C M *Phys. Rev. D* **23** 1693 (1981)
162. Teufel J D et al. *Phys. Rev. Lett.* **101** 197203 (2008)
163. Castellanos-Beltran M A et al. *Nature Phys.* **4** 929 (2008)
164. Teufel J D et al. *Nature Nanotechnol.* **4** 820 (2009)
165. Anetsberger G et al. *Nature Phys.* **5** 909 (2009)
166. Anetsberger G et al. *Phys. Rev. A* **82** 061804(R) (2010)
167. O'Connell A D et al. *Nature* **464** 697 (2010)
168. Blencowe M *Phys. Rep.* **395** 159 (2004)
169. Blair D G et al. *Phys. Rev. Lett.* **74** 1908 (1995)
170. Harry G M et al. *Appl. Phys. Lett.* **76** 1446 (2000)
171. Abbott B et al. (LIGO Sci. Collab.) *Phys. Rev. D* **69** 122001 (2004)
172. Abbott B et al. (LIGO Sci. Collab.) *Phys. Rev. Lett.* **94** 181103 (2005)
173. Abbott B et al. (LIGO Sci. Collab.) *New J. Phys.* **11** 073032 (2009)
174. Yurke B, Kochanski G P *Phys. Rev. B* **41** 8184 (1990)
175. Presilla C, Onofrio R, Bocko M F *Phys. Rev. B* **45** 3735 (1992)
176. Onofrio R, Presilla C *Europhys. Lett.* **22** 333 (1993)
177. White J D *Jpn. J. Appl. Phys.* **32** L1571 (1993)
178. Blencowe M P, Wybourne M N *Physica B* **280** 555 (2000)
179. Zhang Y, Blencowe M P *J. Appl. Phys.* **91** 4249 (2002)
180. Knobel R, Yung C S, Cleland A N *Appl. Phys. Lett.* **81** 532 (2002)
181. Blencowe M P, Wybourne M N *Appl. Phys. Lett.* **77** 3845 (2000)
182. Kirschbaum J et al. *Appl. Phys. Lett.* **81** 280 (2002)
183. Cleland A N et al. *Appl. Phys. Lett.* **81** 1699 (2002)
184. Metzger C H, Karrai K *Nature* **432** 1002 (2004)
185. Kleckner D, Bouwmeester D *Nature* **444** 75 (2006)
186. Poggio M et al. *Phys. Rev. Lett.* **99** 017201 (2007)
187. Schliesser A et al. *Phys. Rev. Lett.* **97** 243905 (2006)
188. Grajcar M et al. *Nature Phys.* **4** 612 (2008)
189. Brown K R et al. *Phys. Rev. Lett.* **99** 137205 (2007)
190. Zhang J, Liu Y, Nori F *Phys. Rev. A* **79** 052102 (2009)
191. Ouyang S-H, You J Q, Nori F *Phys. Rev. B* **79** 075304 (2009)
192. Rabl P et al. *Phys. Rev. B* **79** 041302(R) (2009)
193. Greenberg Ya S, Il ichev E, Nori F *Phys. Rev. B* **80** 214423 (2009)
194. Martin I et al. *Phys. Rev. B* **69** 125339 (2004)
195. Blencowe M P, Imbers J, Armour A D *New J. Phys.* **7** 236 (2005)
196. Clerk A A, Bennett S *New J. Phys.* **7** 238 (2005)
197. Nori F *Nature Phys.* **4** 589 (2008)
198. Grajcar M et al. *Phys. Rev. B* **78** 035406 (2008)
199. Valenzuela S O et al. *Science* **314** 1589 (2006)
200. Hauss J et al. *New J. Phys.* **10** 095018 (2008)
201. Hauss J et al. *Phys. Rev. Lett.* **100** 037003 (2008)
202. Greenberg Ya S *Phys. Rev. B* **76** 104520 (2007)
203. Greenberg Ya S, Il'ichev E *Phys. Rev. B* **77** 094513 (2008)
204. You J Q et al. *Phys. Rev. B* **75** 104516 (2007)
205. You J Q, Liu Y, Nori F *Phys. Rev. Lett.* **100** 047001 (2008)
206. Ashhab S et al. *New J. Phys.* **11** 023030 (2009)
207. Kippenberg T J et al. *Phys. Rev. Lett.* **95** 033901 (2005)
208. Rokhsari H et al. *Opt. Express* **13** 5293 (2005)
209. Carmon T et al. *Phys. Rev. Lett.* **94** 223902 (2005)
210. Arcizet O et al. *Nature* **444** 71 (2006)
211. Gigan S et al. *Nature* **444** 67 (2006)
212. Corbitt Th et al. *Phys. Rev. Lett.* **98** 150802 (2007)
213. Thompson J D et al. *Nature* **452** 72 (2008)
214. Schliesser A et al. *Nature Phys.* **4** 415 (2008)
215. Gröblacher S et al. *Eur. Phys. Lett.* **81** 54003 (2008)
216. Miyakawa O et al. *Phys. Rev. D* **74** 022001 (2006)
217. Buonanno A, Chen Y *Phys. Rev. D* **65** 042001 (2002)
218. Corbitt T et al. *Phys. Rev. A* **73** 023801 (2006)
219. Braginsky V B, Manukin A B *Izmerenie Malykh Sil v Fizicheskikh Eksperimentakh* (Measurement of Weak Forces in Physics Experiments) (Moscow: Nauka, 1974) [Translated into English (Chicago: Univ. of Chicago Press, 1977)]
220. Braginsky V B, Minakova I I *Vestn. Mosk. Univ. Fiz. Astron.* (1) 83 (1964)
221. Manukin A B, Tikhonov M Yu *Vestn. Mosk. Univ. Fiz. Astron.* (5) 584 (1970)
222. Wilson-Rae I et al. *Phys. Rev. Lett.* **99** 093901 (2007)
223. Marquardt F et al. *Phys. Rev. Lett.* **99** 093902 (2007)
224. Marquardt F, Clerk A A, Girvin S M *J. Mod. Opt.* **55** 3329 (2008)
225. Gröblacher S et al. *Nature Phys.* **5** 485 (2009)
226. Schliesser A et al. *Nature Phys.* **5** 509 (2009)
227. Ilchenko V S, Matsko A B *IEEE J. Sel. Topics Quant. Electron.* **12** 15 (2006)
228. Armani D K et al. *Nature* **421** 925 (2003)
229. Schliesser A et al. *New J. Phys.* **10** 095015 (2008)
230. Carmon T, Vahala K J *Phys. Rev. Lett.* **98** 123901 (2007)
231. Rivière R et al. *Phys. Rev. A* **83** 063835 (2011); arXiv:1011.0290
232. Lee K H et al. *Phys. Rev. Lett.* **104** 123604 (2010)
233. Braginsky V B, Gorodetsky M L, Ilchenko V S *Phys. Lett. A* **137** 393 (1989)
234. Park Y-S, Wang H *Nature Phys.* **5** 489 (2009)
235. Kippenberg T J et al. *Appl. Phys. Lett.* **83** 797 (2003)
236. Meystre P et al. *J. Opt. Soc. Am. B* **2** 1830 (1985)
237. Bhattacharya M, Uys H, Meystre P *Phys. Rev. A* **77** 033819 (2008)
238. Bhattacharya M, Giscard P-L, Meystre P *Phys. Rev. A* **77** 030303(R) (2008)
239. Bhattacharya M, Meystre P *Phys. Rev. A* **78** 041801(R) (2008)
240. Favero I, Karrai K *New J. Phys.* **10** 095006 (2008)
241. Jayich A M et al. *New J. Phys.* **10** 095008 (2008)
242. Teufel J D, Regal C A, Lehnert K W *New J. Phys.* **10** 095002 (2008)
243. Rocheleau T et al. *Nature* **463** 72 (2009)
244. Hertzberg J B et al. *Nature Phys.* **6** 213 (2010)